JOURNAL OF GUIDANCE, CONTROL, AND DYNAMICS
Vol. 30, No. 5, September–October 2007

High-α Flight Maneuverability Enhancement of a Fighter Aircraft Using Thrust-Vectoring Control

Özgür Atesoglu*
ASELSAN, Inc., 06011 Ankara, Turkey
and
M. Kemal Özgören†
Middle East Technical University, 06531 Ankara, Turkey

DOI: 10.2514/1.28620

This study focuses on high-α flight maneuverability enhancement of a fighter–bomber aircraft for air combat superiority using thrust-vectoring control. Two basic air superiority maneuvers are studied as test cases, which are the Cobra maneuver with longitudinal motion and the Herbst maneuver with both longitudinal and lateral motions. The necessary mathematical models are built to describe the nonlinear 6-degree-of-freedom flight dynamics, the nonlinear aerodynamics, the engine, and the thrust-vectoring paddles of the aircraft. High-α aerodynamics of the aircraft is studied and the integrated Bihrle–Weissmann chart is plotted to determine the stall effected regions. The method employed to control the aircraft is based on feedback linearization with nonlinear dynamic inversion. Both of the test case maneuvers are simulated with two control modes using aerodynamic control only and thrust-vectoring control only. Then the performances of these control modes are compared. This study demonstrates that an additional thrust-vectoring control system integrated to the conventional aerodynamic flight control system of a fighter aircraft turns out to be highly effective in increasing its high-α maneuvering capability.

Nomenclature

$\boldsymbol{a}_{b/o}$	=	translational acceleration vector of the aircraft
C_i	=	general symbol for aerodynamic force and moment coefficients
$C_{n\beta\text{dyn}}$	=	dynamic sensitivity of yaw moment to side slip angle
$\hat{C}^{(o,b)}$	=	rotation matrix from Earth fixed reference frame to body fixed reference frame
$\boldsymbol{F}_a$, $\boldsymbol{M}_a$	=	aerodynamic force and moment vectors
$\boldsymbol{F}_L$, $\boldsymbol{F}_R$	=	thrust force vectors of the left and right engines
$\bar{F}^{(b)}_{\text{com}}$	=	array of computed force components
f_{nA}	=	natural frequency of the aerodynamic surface actuator dynamics
$f_{n\text{TVC}}$	=	natural frequency of the paddle actuator dynamics
$\boldsymbol{g}$	=	Earth gravity field vector
h	=	altitude of the aircraft
$\hat{I}$	=	identity matrix
$\hat{J}$	=	inertia matrix of the aircraft
$\hat{K}_p$, $\hat{K}_i$, $\hat{K}_d$	=	controller matrix gains
M	=	Mach number
$\bar{M}^{(b)}_{\text{com}}$	=	array of computed moment components
m	=	mass of the aircraft
P_a, P_c	=	actual and commanded power level percentages of the full engine power
p, q, r	=	angular velocity components of the aircraft
$\hat{R}_k(\theta)$	=	rotation matrix of angle θ about the kth axis
$\boldsymbol{r}_{be_L}$, $\boldsymbol{r}_{be_R}$	=	position vectors of the engine nozzle exits with respect to the mass center
$\boldsymbol{r}_{b/o}$	=	position vector of the aircraft
T_L, T_R	=	total thrust created by aircraft engines
T_{mil}, T_{idle}, $T_{\max}$	=	military, idle, and maximum thrust levels
u, v, w	=	translational velocity components of the aircraft in the body fixed frame
$\boldsymbol{u}_1$, $\boldsymbol{u}_2$, $\boldsymbol{u}_3$	=	unit vectors along the body frame axes
V_T	=	total velocity
$\boldsymbol{v}_{b/o}$	=	translational velocity vector of the aircraft
v_s	=	speed of sound
$\bar{X}$	=	column matrix representation of a vector $\boldsymbol{X}$
$\tilde{X}$	=	cross-product matrix corresponding to a vector $\boldsymbol{X}$
$\bar{x}(t)$	=	aircraft states vector
α, β	=	angle of attack and side slip angle
$\boldsymbol{\alpha}_{b/o}$	=	angular acceleration vector of the aircraft
δ_a, δ_e, δ_r	=	aileron, elevator, and rudder deflections
$\delta_{i\text{com}}$	=	general symbol for the computed aerodynamic surface and throttle deflections
δ_{L1}, δ_{L2}, δ_{L3}	=	left engine thrust-vectoring paddle deflections
$\delta_{L\text{th}}$, $\delta_{R\text{th}}$	=	left and right engine throttle deflections
δ_{R1}, δ_{R2}, δ_{R3}	=	right engine thrust-vectoring paddle deflections
θ_L, θ_R	=	elevation deviation of the total thrust of the left and right engines
ρ	=	air density
τ_{eng}	=	time constant of the aircraft engine
ψ, θ, ϕ	=	Euler angles describing the attitude of the aircraft
ψ_L, ψ_R	=	azimuth deviation of the total thrust of the left and right engines
ω_{ni}, ζ_i, ω'_{ni}	=	control parameters of the desired closed-loop dynamics
$\boldsymbol{\omega}_{b/o}$	=	angular velocity vector of the aircraft

I. Introduction

THE fighter aircraft before the 1970s exhibited poor stability characteristics at high angles of attack. The maneuvering was often limited by the airflow departure boundaries, and stall and spin accidents were a major cause of loss of aircraft and pilots [1]. With

Presented as Paper 6056 at the AIAA Guidance, Navigation, and Control Conference and Exhibit, Keystone, Colorado, 21–24 August 2006; received 30 October 2006; revision received 9 February 2007; accepted for publication 12 February 2007.

*Leading Design Engineer, Navigation and Guidance Systems Design Department, Microelectronics, Guidance and Electro-Optics Division.
†Professor, Mechanical Engineering Department.

the emergence of close combat scenarios, it became very important to make certain critical maneuvers rapidly such as evasion, pursuit, and nose pointing to obtain the first opportunity of firing the weapons. Thus, the demand for increased agility and maneuvering led to the necessity of high angle of attack flight. This created the need for the development of research programs such as the X-31A enhanced fighter maneuverability [2,3], F-16 multi-axis thrust vectoring [4], the X-29A vortex flight control system [5], and the NASA High-Alpha Technology Program [6].

The conventional aerodynamic control system requirements are typically specified for low angle of attack conditions. Requirements for high angles of attack are posed only for emergency avoidance from uncontrollable flight. However, the latter requirements are hard to meet because the effectiveness of the aerodynamic control surfaces happens to degrade rapidly at high angles of attack.

The control system configurations for fighter aircraft are primarily based on the criterion of achieving the desired translational and angular accelerations especially for rapid maneuvering tasks. The maneuvering requirements in turn depend primarily on the sizes of the aerodynamic control effectors to provide the necessary control forces and moments for the desired accelerations. This suggests unfeasibly large control effectors in the high-α maneuverability case. Therefore, there is an increasing demand for alternative control effectors such as thrust-vectoring control (TVC) paddles and also for advanced stabilization and control methodologies. Being thus motivated, this study focuses on high-α flight maneuverability enhancement of a fighter aircraft using TVC paddles as additional control effectors and on the controlling technique based on *nonlinear dynamic inversion* (NDI).

II. Fighter Maneuvering Control

The fighter aircraft are required to perform controlled maneuvers well beyond traditional aircraft limits, such as pitch up to a high angle of attack, rapid point to shoot, and other close combat maneuvers. To perform these fast multi-axis motions, most tactical aircraft need the use of innovative technologies such as TVC. The best aircraft for these extreme flight conditions should combine several disciplines successfully in their design phase, for example, nonlinear flight mechanics, unsteady aerodynamics, flexible structural modeling, advanced control theory, and realistic simulation studies.

There is a great technological interest in the area of supermaneuverability. It induces demands on more sophisticated flight control systems with capabilities such as increased usable lift, thrust vectoring, and insensitivity to unsteady aerodynamic effects.

The idea of supermaneuverability was introduced by W. B. Herbst in 1980. He defined supermaneuverability as the capability to execute maneuvers with controlled side slip at angles of attack well beyond those for maximum lift, that is, the capability of post-stall maneuvering. Post-stall maneuvering is flying at very high angles of attack up to 70 deg or even 90 deg for short periods of time. Thus, fighters make drastic changes in direction within extremely short distances and times. A supermaneuverable fighter aircraft can turn faster than a conventional aircraft and dissipate less energy in the process. It can have the adversary aircraft in the field of view of its weapon system earlier than the conventionally controlled aircraft. To make post-stall maneuvering, the aircraft has to be controllable at very high angles of attack. At high angles of attack, the aerodynamic control surfaces lose their effectiveness, the airspeed often becomes quite low, and the vortices in the wake of the stalled wing have a drastic adverse effect on the vertical and horizontal tail surfaces. Therefore, the aerodynamic control surfaces such as rudders and elevators should be accompanied by other controlling techniques such as vectoring the engine thrust.

A. Supermaneuverability and Air Combat Maneuvering

Currently, some modern fighter aircraft are capable of performing transient maneuvers involving high angular velocities at extreme angles of attack. Typical examples for such maneuvers are the so-called Cobra and Herbst (J-turn) maneuvers. The advances on high angle of attack control effectors such as thrust vectoring, side jets, and passive and active aerodynamic control surfaces with different shapes provide greater capability to have an effectively enlarged maneuvering envelope for air combat.

During rapid high angle of attack maneuvers, unsteady aerodynamics effects, which have a crucial impact on the aircraft flight dynamics including stability and control, are extremely important. Because the aircraft is operating in highly nonlinear flow regimes with substantial angular rates, the prediction of departures from stall safe flight and related complex dynamics should receive increased attention. Several studies exist on this area, including development of guidelines for preliminary design [7], improved testing techniques [8], and improved analysis techniques (e.g., prediction of falling leaf motions) [9] and simulation-based predictive capabilities [10].

High angle of attack flight maneuvers primarily address the significance of a high confidence prediction of aircraft dynamics together with modeling and simulation as well as reliable advanced control effectors driven by sophisticated control algorithms to compensate for the loss of airframe stability.

The first step in any aircraft control law design is to determine the required forces and moments that can be realized given the limitations of the control effectors. This can be done conveniently by using the nonlinear dynamic inversion approach [11–13]. This approach depends primarily on the direct manipulation of the equations of motion to generate control laws yielding desired responses for the achievement of the desired maneuver. The controlled outputs are generally taken as the angular body rates but the angle of attack and the side slip angle are also carefully monitored.

B. Nonlinear Dynamic Inversion

NDI is a widely used nonlinear control method, popular in mechanical system design, robotics, and vehicle control. Different names are being used for this method such as computed torque or force method, feedback linearization, etc. However, they all mean the same mathematical approach. The theoretical background on this approach is extensively investigated in different control system design books [14].

NDI is also used extensively in designing flight control systems [15–18]. This controller design technique uses the information about the nonlinear dynamics of the aircraft. The resulting nonlinear controller is valid for the whole flight envelope and therefore there is no need to apply any gain scheduling technique. Other important features of this design technique can be stated as the decoupling of the longitudinal dynamics from the lateral dynamics even at a high-α flight [19], the consequent facility of independent assignment of closed-loop dynamics for each output channel [20], and the simplicity in designing the controllers for the decoupled output channels.

The central idea of dynamic inversion is based on linearizing the dynamics by using appropriate nonlinear terms in the feedback inputs to the system. This approach algebraically transforms a nonlinear system dynamics into a linear one so that linear control techniques can be applied. This is different from the conventional linearization based on the *Jacobian approach*. In feedback linearization, an exact state transformation is considered, which is based on transforming the original system model into an equivalent model of a simpler linear form.

In general, the dynamics of an air vehicle can be expressed as

$$\dot{\bar{x}} = \bar{f}(\bar{x}) + \hat{B}(\bar{x})\bar{u} \tag{1}$$

$$\bar{y} = \bar{h}(\bar{x}) \tag{2}$$

Here $\bar{x} \in \Re^n$ is the state vector, $\bar{u} \in \Re^m$ is the control vector, $\bar{y} \in \Re^m$ is the output vector, $m < n$, $\bar{f}(\bar{x})$, $\hat{B}(\bar{x})$, and $\bar{h}(\bar{x})$ are nonlinear state-dependent functions. To obtain the direct relationship between $\bar{y}$ and $\bar{u}$, $\bar{y}$ is differentiated until the control input appears explicitly in the expression. In case of an aircraft, only one

differentiation happens to be enough to reach such an explicit relationship. That is,

$$\dot{\bar{y}} = [\partial \bar{h}(\bar{x})/\partial(\bar{x})]\dot{\bar{x}} = [\partial \bar{h}(\bar{x})/\partial(\bar{x})]\bar{f}(\bar{x}) + [\partial \bar{h}(\bar{x})/\partial(\bar{x})]\hat{B}(\bar{x})\bar{u} \quad (3)$$

If $[\partial \bar{h}(\bar{x})/\partial(\bar{x})]\hat{B}(\bar{x})$ is invertible for all values of $\bar{x}$, then the inverse dynamics linearization is achieved by means of the following transformation:

$$\bar{u} = \bar{u}(\bar{x}, \bar{r}) = \{[\partial \bar{h}(\bar{x})/\partial(\bar{x})]\hat{B}(\bar{x})\}^{-1}\{\bar{r} - [\partial \bar{h}(\bar{x})/\partial(\bar{x})]\bar{f}(\bar{x})\} \quad (4)$$

This transformation converts Eq. (3) into the following simple and linear form:

$$\dot{\bar{y}} = \bar{r} \quad (5)$$

Here $\bar{r}$ is the auxiliary control vector, which is used as the command vector on $\dot{\bar{y}}$ to force $\bar{y}$ to track a desired output vector $\bar{y}_d(t)$. It can be generated to impose the desired motion to the aircraft. In general, proportional (P) or proportional plus integral (PI) control laws turn out to be quite satisfactory for this purpose. In other words, $\bar{r}$ can be generated in one of the following ways expressed by Eqs. (6a) and (6b):

$$\bar{r}(t) = \omega_{nd}[\bar{y}_d(t) - \bar{y}(t)] \quad (6a)$$

$$\bar{r}(t) = 2\zeta_d\omega_{nd}[\bar{y}_d(t) - \bar{y}(t)] + \omega_{nd}^2\int_0^t [\bar{y}_d(s) - \bar{y}(s)]\,\mathrm{d}s \quad (6b)$$

It is also very important that, if $\dim(\bar{y}) < \dim(\bar{x})$, which is so in general, the control action described above (which constitutes an outer loop for tracking purposes) may not be sufficient to stabilize the whole system. In that case, it will be necessary to use an additional inner control loop with state variable feedback for sake of stability augmentation.

Here ω_{nd} is the desired natural frequency, and ζ_d is the desired damping coefficient of the closed-loop dynamics. After the auxiliary control $\bar{r}$, to generate the actual control $\bar{u}$ according to Eq. (4), the state vector $\bar{x}$ has to be completely available and $\{[\partial \bar{h}(\bar{x})/\partial(\bar{x})]\hat{B}(\bar{x})\}$ should be invertible for all values of $\bar{x}$. On the other hand, when it is invertible but has a small determinant, the control vector becomes large and the actuators may saturate. If this is the case and PI control law is used it is necessary to use an antiwindup scheme and minimize the integral gain to control the accumulation of the error in the integral term.

The nonlinear dynamic inversion is actually a special case of the *model following technique* [21]. Similar to other model following controllers, an NDI controller requires exact knowledge of the system dynamics to achieve a satisfactory performance. Therefore, robustness has a significant role during the design process. In the presence of parameter uncertainty and/or unmodeled dynamics, the robustness of the system may not be guaranteed. The unmodeled dynamics is very important, because the exact model of the system is never available in practice. Moreover, the sensitivity to modeling errors may be particularly severe when the linearizing transformation happens to be poorly conditioned. In this paper, the model of the system is assumed to be perfect.

III. Modeling the Fighter–Bomber Aircraft

A. Modeling the Aircraft Dynamics During the TVC Phase

In the process of dynamic modeling, the aircraft is assumed to be rigid with practically constant mass and density and symmetric about its x–z plane. It is also assumed that the gyroscopic effects of the rotating engine parts are negligible. The undeflected thrust force of each engine is assumed to act parallel to the longitudinal body axis. However, it can be deviated as desired by using the thrust-vectoring paddles.

Dynamic modeling of the aircraft is started by defining two reference frames: the Earth fixed reference frame (assumed to be inertial) and the body fixed reference frame attached to the mass center of the aircraft. The two control forces (i.e., the forces obtained by thrust deviations) in the TVC phase are denoted by $\boldsymbol{F}_L$ and $\boldsymbol{F}_R$, which are applied at arbitrary directions at different locations. These locations are defined with respect to the origin of the body fixed reference frame by the position vectors $\boldsymbol{r}_{be_L}$ and $\boldsymbol{r}_{be_R}$. Note that the aerodynamic forces and moments are treated as disturbances in this phase. The position of the aircraft with respect to the Earth fixed reference frame is defined by the vector $\boldsymbol{r}_{ob}$. Figure 1 shows the mentioned reference frames, actuation forces with their locations, and the aerodynamic forces and moments on the aircraft.

The rotational transformation between the Earth fixed reference frame and the body fixed reference frame is defined by three successive rotations. These three rotations are defined by the *Euler angles* ψ, θ, and ϕ. $\hat{C}^{(o,b)}$ is the rotation matrix from the Earth fixed reference frame to the body fixed reference frame. The angular velocity of the aircraft with respect to the Earth fixed reference frame, that is, $\boldsymbol{\omega}_{b/o}$, can be expressed in the body fixed frame as follows, where s and c are used to denote the sine and cosine functions for sake of brevity:

$$\bar{\omega}_{b/o}^{(b)} = (\dot{\phi} - \dot{\psi}s\theta)\bar{u}_1 + (\dot{\theta}c\phi + \dot{\psi}c\theta s\phi)\bar{u}_2 + (\dot{\psi}c\theta c\phi - \dot{\theta}s\phi)\bar{u}_3 \quad (7)$$

If the angular velocity components in the body fixed reference frame are denoted as p, q, and r, then $\bar{\omega}_{b/o}^{(b)}$ can also be written as

$$\bar{\omega}_{b/o}^{(b)} = \begin{bmatrix} p \\ q \\ r \end{bmatrix} = \begin{bmatrix} 1 & 0 & -s\theta \\ 0 & c\phi & c\theta s\phi \\ 0 & -s\phi & c\theta c\phi \end{bmatrix}\begin{bmatrix} \dot{\phi} \\ \dot{\theta} \\ \dot{\psi} \end{bmatrix} \quad (8)$$

The translational acceleration $\boldsymbol{a}_{b/o}$ of the aircraft with respect to the Earth fixed reference frame can be found by differentiating its translational velocity vector, which is expressed in the body fixed frame as $\boldsymbol{v}_{b/o} = u\boldsymbol{u}_1^{(b)} + v\boldsymbol{u}_2^{(b)} + w\boldsymbol{u}_3^{(b)}$. Hence $\bar{a}_{b/o}^{(b)} = \dot{\bar{v}}_{b/o}^{(b)} + \tilde{\omega}_{b/o}^{(b)}\bar{v}_{b/o}^{(b)}$, and in detailed form it can be written as

$$\bar{a}_{b/o}^{(b)} = \begin{bmatrix} \dot{u} \\ \dot{v} \\ \dot{w} \end{bmatrix} + \begin{bmatrix} 0 & -r & q \\ r & 0 & -p \\ -q & p & 0 \end{bmatrix}\begin{bmatrix} u \\ v \\ w \end{bmatrix} \quad (9)$$

Because V_T, α, and β can be measured directly on the aircraft and have a direct relationship to piloting, it is preferable to write the translational equations in terms of the wind frame variables. For this purpose, let $\bar{v}_{b/o}^{(w)} = V_T\bar{u}_1$, so that $\bar{v}_{b/o}^{(b)} = V_T\hat{C}^{(b,w)}\bar{u}_1$. Then, differentiating $\bar{v}_{b/o}^{(b)}$, the acceleration of the aircraft with respect to the Earth fixed reference frame can be found as follows with its expression in the body fixed frame:

$$\bar{a}_{b/o}^{(b)} = \dot{V}_T\hat{C}^{(b,w)}\bar{u}_1 + V_T\dot{\hat{C}}^{(b,w)}\bar{u}_1 + V_T\tilde{\omega}_{b/o}^{(b)}\hat{C}^{(b,w)}\bar{u}_1 \quad (10)$$

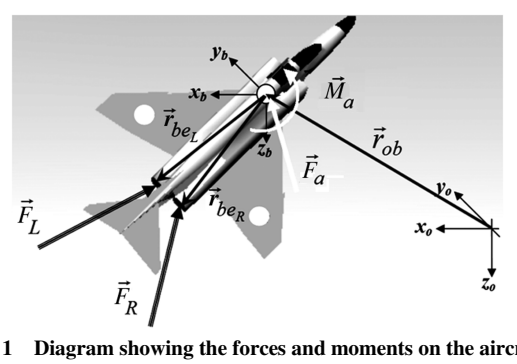

Fig. 1 Diagram showing the forces and moments on the aircraft.

Here $\hat{C}^{(b,w)}$ is expressed as in the following equation:

$$\hat{C}^{(b,w)} = \begin{bmatrix} c\alpha c\beta & -c\alpha s\beta & -s\alpha \\ s\beta & c\beta & 0 \\ s\alpha c\beta & -s\alpha s\beta & c\alpha \end{bmatrix} \tag{11}$$

Hence, using Eqs. (9–11), the relation between the wind frame variables and the body frame variables of the translational acceleration can be found.

$$\begin{bmatrix} \dot{u} \\ \dot{v} \\ \dot{w} \end{bmatrix} = \begin{bmatrix} c\alpha c\beta & -V_T s\alpha c\beta & -V_T c\alpha s\beta \\ s\beta & 0 & V_T c\beta \\ s\alpha c\beta & V_T c\alpha c\beta & -V_T s\alpha s\beta \end{bmatrix} \begin{bmatrix} \dot{V}_T \\ \dot{\alpha} \\ \dot{\beta} \end{bmatrix} \tag{12}$$

The six nonlinear rigid-body equations of motion are derived using the *Newton–Euler equations*. In these equations, the mass of the aircraft is denoted with m, the inertia tensor of the aircraft is expressed by the matrix $\hat{J} = \hat{J}^{(b)}$ in the body fixed frame, the Earth gravity field vector is denoted with $\boldsymbol{g}$, and the aerodynamic force and moment vectors created on the aircraft during its flight are denoted with $\boldsymbol{F}_a$ and $\boldsymbol{M}_a$. $\boldsymbol{F}_L$ and $\boldsymbol{F}_R$ are the thrust force vectors of the two engines with magnitudes T_L and T_R. Their azimuth and elevation angles with respect to the body fixed reference system are denoted by the pairs $\{\psi_L, \psi_R\}$ and $\{\theta_L, \theta_R\}$. The force equation can be written in the body fixed frame as

$$m\bar{a}_{b/o}^{(b)} = m\dot{\bar{v}}_{b/o}^{(b)} + m\tilde{\omega}_{b/o}^{(b)}\bar{v}_{b/o}^{(b)} = \bar{F}_L^{(b)} + \bar{F}_R^{(b)} + mg\hat{C}^{(b,o)}\bar{u}_3 + \bar{F}_a^{(b)} \tag{13}$$

Here $\bar{F}_L^{(b)} = T_L\hat{R}_3(\psi_L)\hat{R}_2(\theta_L)\bar{u}_1$ and $\bar{F}_R^{(b)} = T_R\hat{R}_3(\psi_R)\hat{R}_2(\theta_R)\bar{u}_1$. Similarly, the moment equation can be written in the body fixed frame as

$$\hat{J}\bar{\alpha}_{b/o}^{(b)} = -\tilde{\omega}_{b/o}^{(b)}\hat{J}\bar{\omega}_{b/o}^{(b)} + \tilde{r}_{be_L}^{(b)}\bar{F}_L^{(b)} + \tilde{r}_{be_R}^{(b)}\bar{F}_R^{(b)} + \bar{M}_a^{(b)} \tag{14}$$

Finally, the Newton–Euler equations describing the rigid-body motion of the aircraft can be combined into a single augmented matrix equation as

$$\begin{bmatrix} \begin{bmatrix} \dot{u} & \dot{v} & \dot{w} \end{bmatrix}^T \\ \begin{bmatrix} \dot{p} & \dot{q} & \dot{r} \end{bmatrix}^T \end{bmatrix} = \bar{F} + \hat{H}\left\{\hat{G}\begin{bmatrix} \bar{F}_L^{(b)} \\ \bar{F}_R^{(b)} \end{bmatrix} + \begin{bmatrix} \bar{F}_a^{(b)} \\ \bar{M}_a^{(b)} \end{bmatrix}\right\} \tag{15}$$

Here the matrices $\bar{F}$, $\hat{G}$, and $\hat{H}$ are used for shorthand notation. They are defined as follows:

$$\bar{F} = \begin{bmatrix} -\tilde{\omega}_{b/o}^{(b)}\bar{v}_{b/o}^{(b)} + g\hat{C}^{(b,o)}\bar{u}_3 \\ -\hat{J}^{-1}\tilde{\omega}_{b/o}^{(b)}\hat{J}\bar{\omega}_{b/o}^{(b)} \end{bmatrix}, \qquad \hat{G} = \begin{bmatrix} \hat{I} & \hat{I} \\ \tilde{r}_{be_L}^{(b)} & \tilde{r}_{be_R}^{(b)} \end{bmatrix}$$
$$\hat{H} = \begin{bmatrix} \hat{I}/m & 0 \\ 0 & \hat{J}^{-1} \end{bmatrix} \tag{16}$$

In these expressions, $\hat{I}$ is the 3×3 identity matrix.

B. Modeling the Aircraft Aerodynamics

1. *High Angle of Attack Behavior*

High angle of attack aerodynamics are inherently associated with separated flows and nonlinear aerodynamics. Studies on high angle of attack aerodynamics are heavily dependent on wind tunnel and flight testing. The data generated from these tests are used to construct an aerodynamic model of the aircraft. Such a model is important in that it should represent the major design concerns for a supermaneuverable fighter aircraft. The important design concerns are 1) ability to control the aircraft at high angle of attack maneuvering, 2) flight without departure when the pilot is in the loop, and 3) allowance for nearly unlimited angle of attack range.

2. *Departure Indication Parameters*

The studies on unsteady aerodynamics indicated two important parameters of departure and stall phenomena. They are $C_{n\beta\text{dyn}}$ and LCDP (lateral control departure parameter). $C_{n\beta\text{dyn}}$ is known as a convenient stall predictor, but it only indicates an approximate tendency to stall. Because it does not contain any aerodynamic terms related to the control surfaces, it is an open loop parameter. $C_{n\beta\text{dyn}}$ is a combination of the lateral and directional moment affectivities as a function of the angle of attack and the inertia ratio in the x–z plane of the aircraft. For a safe and stall free region, it should have a positive value. As for LCDP, it seems to be a better predictor to indicate the tendency to departure and stall. This is because it is not an open loop parameter, since it contains aerodynamic terms related to the ailerons in addition to the lateral and directional moment affectivities. For a safe and stall free region, LCDP should also have a positive value. Negative values imply roll reversal. The expressions for these stall susceptibility indicators are given as

$$C_{n\beta\text{dyn}} = C_{n\beta}\cos(\alpha) - (J_z/J_x)C_{l\beta}\sin(\alpha) \tag{17a}$$

$$\text{LCDP} = C_{n\beta} - C_{l\beta}(C_{n\delta_a}/C_{l\delta_a}) \tag{17b}$$

Here $C_{n\beta}$ and $C_{l\beta}$ are the sensitivities of the yaw and roll moments to the side slip angle, respectively, and J_z and J_x are the inertia components of the aircraft along the z and x directions of the body fixed frame.

Bihrle and Weissmann proposed a chart that indicates the regions in which the aircraft will encounter spin, roll reversal, and departure from controlled flight. This chart is shown in Fig. 2. On this chart, region A implies a high resistance to both departure and spin. Region B implies a considerable resistance to spin but it also implies occurrence of roll reversals that induce departure and post-stall gyrations. Region C implies a weak tendency for spin and occurrence of strong roll reversals inducing departures. Different from region C, the spin tendency is also strong in region D. Region E implies a weak tendency for spin and a moderate tendency for departure. Region F implies a weak resistance to both departure and spin. It also implies that roll reversals do not occur. Finally, region U is characterized by high directional instability.

3. *Nonlinear Modeling of the Aircraft Aerodynamics*

The two-seat all-weather fighter–bomber aircraft considered in this study is fitted with a low-mounted swept wing with wingtip dihedral. The tail section consists of an all-moving horizontal stabilator placed in a cathedral configuration and a single vertical tail. The trailing edge of the main wing contains the control surfaces acting as ailerons and flaps. The trailing edge of the vertical tail has a rudder control surface. Thrust is provided by two afterburning jet

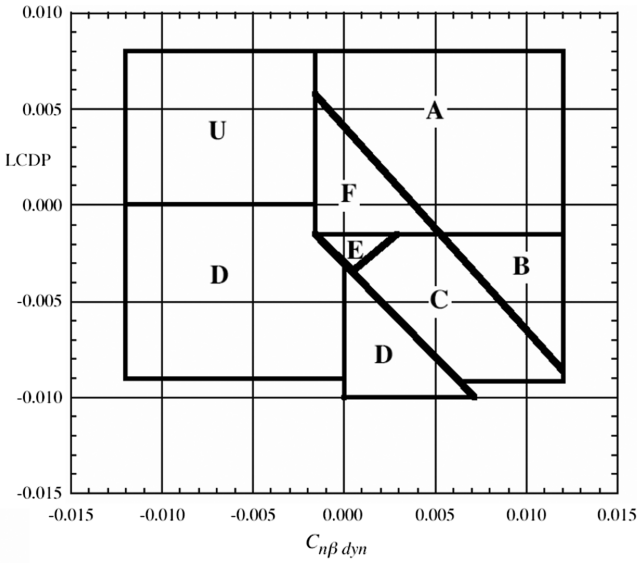

Fig. 2 Regions of the integrated Bihrle–Weissmann chart.

engines mounted on the left and right sides of the rear part of the fuselage.

The simulation model built for this study is aerodynamically controlled with the elevator, aileron, and rudder actions. The deflections of these aerodynamic control surfaces are denoted by δ_e, δ_a, and δ_r, respectively. The left and right engine thrusts are controlled by using the engine throttle deflections denoted by $\delta_{L\text{th}}$ and $\delta_{R\text{th}}$. The aerodynamic data, which are used in the simulation model, are gathered assuming that the ground effect is absent, the landing gears are retracted, and there are no external stores. Aerodynamics is modeled in terms of polynomial functions that involve the control surface deflections, the angle of attack, the side slip angle, and the angular velocity components in the body fixed reference frame. Polynomial fits for each of the nondimensional aerodynamic force and moment coefficients are valid over an angle of attack range of $-15 \leq \alpha \leq 55$ deg. Aerodynamic coefficients are referenced to an assumed center of gravity location originated from the technical documentary of the aircraft. The yaw and pitch moment coefficients C_n and C_m include a correction for the center of gravity position. This is considered to account for the effect of changing the center of gravity position due to fuel consumption during the flight. The control surface deflections are assumed to be limited as follows: $-21 < \delta_e < 7$ deg, $-16 \leq \delta_a \leq 16$ deg, and $-30 < \delta_r < 30$ deg. Any limitation on the side slip angle is not mentioned in the model.

The nondimensional aerodynamic force and moment coefficients for the aircraft model vary nonlinearly with the angles α and β, the angular velocity components p, q, r, and the control surface deflections δ_e, δ_a, and δ_r. The coefficients are computed as shown in Eqs. (18–23) for the region $-15 \leq \alpha \leq 15$ deg. Similar detailed equations are also available [22] for the regions $15 < \alpha < 30$ deg and $30 \leq \alpha \leq 55$ deg, but they are not displayed here due to space limitation. For $\alpha > 55$ deg, the same aerodynamic coefficient equations as those for $30 \leq \alpha \leq 55$ deg are used.

Using the aerodynamic coefficient functions, the stall analysis of the aircraft is made and the stall indication parameters are presented as shown in Fig. 3. Studies on the aerodynamic coefficients have shown that the lift coefficient decreases after $\alpha = 31$ deg. As another point, although the elevator is kept at -21 deg to produce a positive pitching moment, the pitching moment changes sign after $\alpha = 27$ deg. However, unfortunately $C_{n\beta\text{dyn}}$ and LCDP have negative values even after a not so large α such as $\alpha = 20$ deg.

As Fig. 3 is examined, it is seen that region A, that is, the safest region, is encountered for $-15 \leq \alpha \leq 17$ deg. As the angle of attack increases further, weak spin resistance, roll reversals, and departures can be seen. After $\alpha = 22$ deg roll reversals and departures become more effective and the control effectiveness parameters gradually decrease. This study reveals that $\alpha = 22$ deg is the critical angle of attack value after which the stall tendency starts to show up.

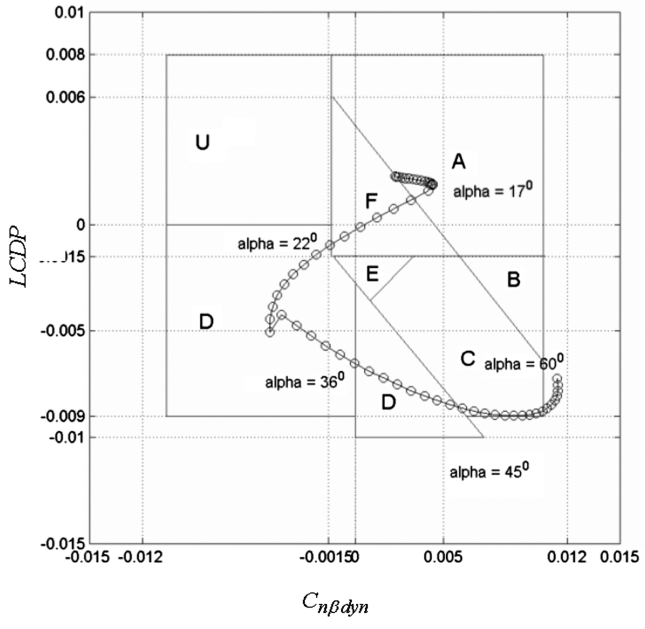

Fig. 3 Integrated Bihrle–Weissmann chart for the aircraft.

$$C_X = 0.0434 + 2.39 \times 10^{-3}\alpha + 2.53 \times 10^{-5}\beta^2 - 1.07 \times 10^{-6}\alpha\beta^2 + 9.5 \times 10^{-1}\delta_e - 8.5 \times 10^{-7}\delta_e\beta^2 + \left(\frac{180q\bar{c}}{\pi 2V_t}\right)(8.73 \times 10^{-3} + 0.001\alpha - 1.75 \times 10^{-4}\alpha^2) \tag{18}$$

$$C_Y = -0.012\beta + 1.55 \times 10^{-3}\delta_r - 8 \times 10^{-6}\delta_r\alpha + \left(\frac{180b}{\pi 2V_t}\right)(2.25 \times 10^{-3}p + 0.0117r - 3.67 \times 10^{-4}r\alpha + 1.75 \times 10^{-4}r\delta_e) \tag{19}$$

$$C_Z = -0.131 - 0.0538\alpha - 4.76 \times 10^{-3}\delta_e - 3.3 \times 10^{-5}\delta_e\alpha - 7.5 \times 10^{-5}\delta_a^2 + \left(\frac{180q\bar{c}}{\pi 2V_t}\right)(-0.111 + 5.17 \times 10^{-3}\alpha - 1.1 \times 10^{-3}\alpha^2) \tag{20}$$

$$C_l = -5.98 \times 10^{-4}\beta - 2.83 \times 10^{-4}\alpha\beta + 1.51 \times 10^{-5}\alpha^2\beta - \delta_a(6.1 \times 10^{-4} + 2.5 \times 10^{-5}\alpha - 2.6 \times 10^{-6}\alpha^2) - \delta_r(-2.3 \times 10^{-4} + 4.5 \times 10^{-6}\alpha) + \left(\frac{180b}{\pi 2V_t}\right) \times (-4.12 \times 10^{-3}p - 5.24 \times 10^{-4}p\alpha + 4.36 \times 10^{-5}p\alpha^2 + 4.36 \times 10^{-4}r + 1.05 \times 10^{-4}r\alpha + 5.24 \times 10^{-5}r\delta_e) \tag{21}$$

$$C_m = -6.61 \times 10^{-3} - 2.67 \times 10^{-3}\alpha - 6.48 \times 10^{-5}\beta^2 - 2.65 \times 10^{-6}\alpha\beta^2 - 6.54 \times 10^{-3}\delta_e - 8.49 \times 10^{-5}\delta_e\alpha + 3.74 \times 10^{-6}\delta_e\beta^2 3.5 \times 10^{-5}\delta_a^2 + \left(\frac{180q\bar{c}}{\pi 2V_t}\right) \times (-0.0473 - 1.57 \times 10^{-3}\alpha) + (x_{c.g.,\text{ref}} - x_{c.g.})C_Z \tag{22}$$

$$C_n = 2.28 \times 10^{-3}\beta + 1.79 \times 10^{-6}\beta^3 + 1.4 \times 10^{-5}\delta_a + 7.0 \times 10^{-6}\delta_a\alpha - 9.0 \times 10^{-4}\delta_r + 4.0 \times 10^{-6}\delta_r\alpha + \left(\frac{180b}{\pi 2V_t}\right)(-6.63 \times 10^{-5}p - 1.92 \times 10^{-5}p\alpha + 5.06 \times 10^{-6}p\alpha^2 - 6.06 \times 10^{-3}r - 8.73 \times 10^{-5}r\delta_e + 8.7 \times 10^{-6}r\delta_e\alpha) - \left(\frac{\bar{c}}{b}\right)(x_{c.g.,\text{ref}} - x_{c.g.})C_Y \tag{23}$$

C. Modeling the Aircraft Engines

Each engine of the aircraft is modeled as a first-order dynamic system with the following response equation to a commanded power demand:

$$\dot{P}_a = (1/\tau_{\text{eng}})(P_c - P_a) \tag{24}$$

P_c is computed as a function of the throttle position as described below and the engine time constant τ_{eng} is scheduled as also described below to achieve a satisfactory engine dynamics. The

thrust forces of each engine are typically determined as a function of the actual power percentage, the altitude, and the Mach number for idle, military, and maximum power settings [23].

As mentioned above, the commanded power percentage is computed as a function of the throttle position δ_{th} as follows:

$$P_c(\delta_{\text{th}}) = \begin{cases} (64.94)\delta_{\text{th}} & \text{if } \delta_{\text{th}} \le 0.77 \\ (217.38)\delta_{\text{th}} - 117.38 & \text{if } \delta_{\text{th}} > 0.77 \end{cases} \tag{25}$$

As for the engine time constant τ_{eng}, it is scheduled as a function of P_c as follows:

$$1/\tau_{\text{eng}} = \begin{cases} 5 & \text{if } P_c \ge 50 \quad \text{and} \quad P_a \ge 50 \\ (1/\tau_{\text{eng}})^* & \text{if } P_c \ge 50 \quad \text{and} \quad P_a < 50 \\ 5 & \text{if } P_c < 50 \quad \text{and} \quad P_a \ge 50 \\ (1/\tau_{\text{eng}})^* & \text{if } P_c < 50 \quad \text{and} \quad P_a < 50 \end{cases} \tag{26}$$

where

$$(1/\tau_{\text{eng}})^* = \begin{cases} 1 & \text{if } (P_c - P_a) \le 25 \\ 0.1 & \text{if } (P_c - P_a) \ge 50 \\ 1.9 - 0.036(P_c - P_a) & \text{if } 25 < (P_c - P_a) < 50 \end{cases} \tag{27}$$

Finally, the resultant total thrust can be estimated using the following approximate formula, which involves the idle, military, and maximum thrust values as well as the actual power percentage of the engines:

$$T_{\text{tot}} = \begin{cases} T_{\text{idle}}(M,h) + (T_{\text{mil}}(M,h) - T_{\text{idle}}(M,h))\left(\frac{P_a}{50}\right) & \text{if } P_a < 50 \\ T_{\text{mil}}(M,h) + (T_{\text{max}}(M,h) - T_{\text{mil}}(M,h))\left(\frac{P_a - 50}{50}\right) & \text{if } P_a \ge 50 \end{cases} \tag{28}$$

D. Modeling the Flight Environment of the Aircraft

In the simulations, a stationary atmosphere is assumed and thus the wind, gust, and burst effects are not included. The air density (ρ) and the speed of sound (v_s) are calculated using the ICAO model of the standard atmosphere. According to this model, $\rho = \rho_0(1 - 0.00002256h^{4.256})$ and $v_s = (\gamma RT)^{1/2}$. Here, $\gamma = 1.4$, R is the specific gas constant, ρ_0 is the air density at the sea level, and T is the ambient temperature of the surrounding air, which is expressed as $T = T_0(1 - 0.00002256h)$, where T_0 is the ambient temperature at the sea level. The Mach number is expressed as $M = V_T/v_s$ and the dynamic pressure is expressed as $Q_d = (1/2)\rho V_T^2$, where V_T is the speed of the aircraft.

The curvature of the Earth is ignored and the Earth fixed reference frame is assumed to be inertial. It is also assumed that the gravity field is uniform, that is, g is constant.

E. Modeling the Thrust-Vectoring Paddles

Thrust-vectoring applications encountered in some research and development programs focused on vectoring either in the pitch plane to improve the pitch control performance or in the yaw plane to improve the yaw control performance. There are also typical research aircrafts integrated with thrust-vectoring both in the pitch and yaw planes. These aircrafts are X-31A and NASA F-18 HARV. Both aircrafts are fitted with a thrust-vectoring system that employs three postexit vanes radially displaced about their axisymmetric nozzles.

The fighter–bomber aircraft considered in this study does not originally have the capability of thrust-vectoring. Therefore, it is assumed that it is also virtually fitted with a similar thrust-vectoring system as those that are used for the X-31A and NASA F-18 HARV aircrafts.

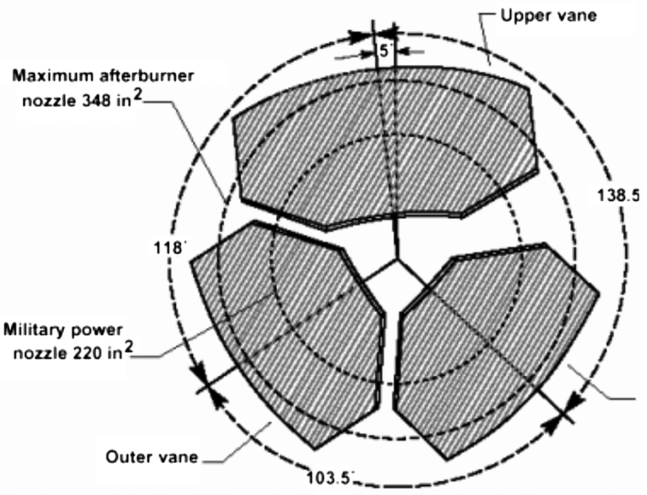

Fig. 4 Vane configuration for one engine of the HARV aircraft.

Figure 4 shows the vane configuration for one engine of the HARV aircraft [24].

For the longitudinal and lateral planes of motion, the maximum jet turning angle envelope, where at least one vane is deflected to 30 deg, is shown in Fig. 5. As noted, the envelope contours are not affected by different values of nozzle pressure ratio (NPR), that is, the ratio of the air pressure at the outlet of the nozzle to the ambient pressure.

Throughout this study, a jet turning envelope similar to that of the HARV aircraft is generated for the modeling purposes. In that generic envelope different nozzle pressure ratios and engine power settings are neglected.

The virtually fitted thrust-vectoring system has three thrust-vectoring paddles on each of the right and left engines. Therefore, thrusts of the right and left engines can be deviated individually. A hexagonal shaped envelope is generated to define the transformation between the thrust-vectoring paddle deflections and the resultant thrust deviation angles. All three paddles of an engine are assumed to deflect 30 deg at most. The generated envelope is shown in Fig. 6.

Because the envelope is hexagonally shaped, maximum deflections of the three paddles lead to different maximum values of lateral and longitudinal thrust deviations which are 30 deg for pitch and 20 deg for yaw, respectively. On the other hand, if the resultant pitch deflections are in between 15 and 30 deg, maximum yaw deflections should be less than 20 deg. The equations, for the left

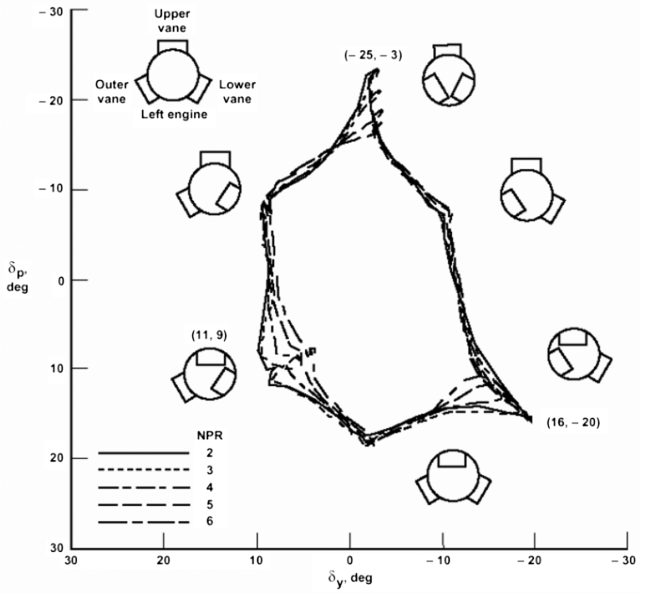

Fig. 5 Maximum jet turning angle envelope for HARV.

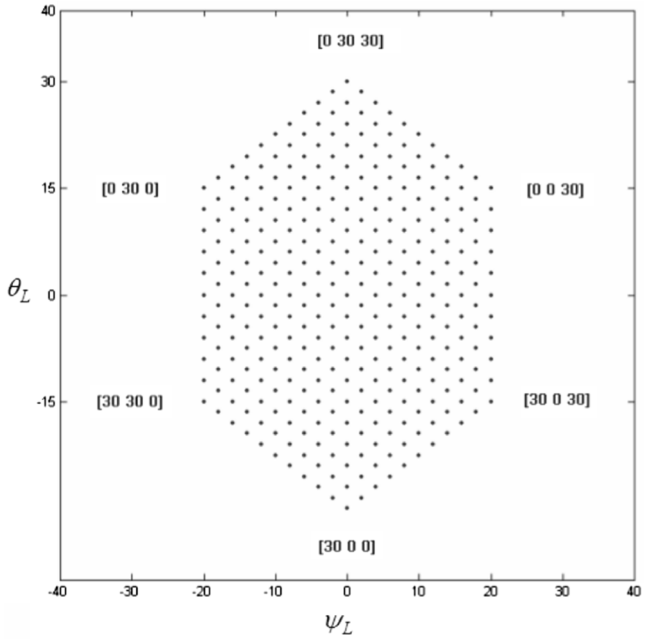

Fig. 6 Maximum jet turning angle envelope.

engine, defining the transformation between the thrust-vectoring paddle deflections and the resultant thrust deviation angles are shown through Eqs. (29–32):

$$\begin{bmatrix} \theta_L \\ \psi_L \end{bmatrix} = \begin{bmatrix} -(30/30) & (1/2)(30/30) & (1/2)(30/30) \\ 0 & (20/30) & -(20/30) \end{bmatrix} \begin{bmatrix} \delta_{L1} \\ \delta_{L2} \\ \delta_{L3} \end{bmatrix} \tag{29}$$

$$\begin{bmatrix} \theta_L \\ \psi_L \end{bmatrix} = \begin{bmatrix} 1/2 & 1/2 \\ 2/3 & -2/3 \end{bmatrix} \begin{bmatrix} \delta_{L2} \\ \delta_{L3} \end{bmatrix} - \begin{bmatrix} \delta_{L1} \\ 0 \end{bmatrix} \tag{30}$$

$$\begin{bmatrix} \delta_{L2} \\ \delta_{L3} \end{bmatrix} = \begin{bmatrix} 1/2 & 1/2 \\ 2/3 & -2/3 \end{bmatrix}^{-1} \left\{ \begin{bmatrix} \theta_L \\ \psi_L \end{bmatrix} + \begin{bmatrix} \delta_{L1} \\ 0 \end{bmatrix} \right\} \tag{31}$$

$$\begin{bmatrix} \delta_{L2} - \delta_{L1} \\ \delta_{L3} - \delta_{L1} \end{bmatrix} = \begin{bmatrix} \theta_L + (3/4)\psi_L \\ \theta_L - (3/4)\psi_L \end{bmatrix} \tag{32}$$

From Eq. (31) it is seen that δ_{L1}, δ_{L2}, and δ_{L3} cannot be solved independently. Only the differences $\delta_{L2} - \delta_{L1}$ and $\delta_{L3} - \delta_{L1}$ can be solved. The proposed solution method is as follows: $\delta_{L2} - \delta_{L1}$ and $\delta_{L3} - \delta_{L1}$ are found by assigning a proper value to δ_{L1}. This value is assigned as follows:

$$\begin{aligned} &\text{if } (\delta_{L2} < 0 \text{ deg}) \text{ and } (\delta_{L3} > 0 \text{ deg}) \text{ then } && \delta_{L1} = |\delta_{L2}| \\ &\text{if } (\delta_{L3} < 0 \text{ deg}) \text{ and } (\delta_{L2} > 0 \text{ deg}) \text{ then } && \delta_{L1} = |\delta_{L3}| \\ &\text{if } (\delta_{L3} < 0 \text{ deg}) \text{ and } (\delta_{L2} > 0 \text{ deg}) \text{ then } && \delta_{L1} = \max(|\delta_{L2}|, |\delta_{L3}|) \end{aligned} \tag{33}$$

It can be seen in Fig. 6 that $\psi_{L\max}$ decreases with increasing θ_L in the range between 15 and 30 deg. Thus, all three paddle deflections will be positive and limited in the range between and 0 and 30 deg. This is implemented as follows:

$$|\psi_{L\max}| = \begin{cases} 20 \text{ deg} & \text{if } |\theta_L| < 15 \text{ deg} \\ 20 \text{ deg}(1 - (|\theta_L| - 15)/15 \text{ deg}) & \text{if } 15 \le |\theta_L| \le 30 \text{ deg} \end{cases} \tag{34}$$

As for the mechanization, the three thrust-vectoring paddles are actuated independently and the actuation dynamics is modeled simply as follows:

$$\begin{bmatrix} \dot{\delta}_{L1} \\ \dot{\delta}_{L2} \\ \dot{\delta}_{L3} \end{bmatrix} = (2\pi f_{n\text{TVC}}) \left\{ \begin{bmatrix} \delta_{L1\text{com}} \\ \delta_{L2\text{com}} \\ \delta_{L3\text{com}} \end{bmatrix} - \begin{bmatrix} \delta_{L1} \\ \delta_{L2} \\ \delta_{L3} \end{bmatrix} \right\} \tag{35}$$

Here the commanded (com) values are determined by the preceding equations and $f_{n\text{TVC}} = 30$ Hz. To ensure the physical limits of the thrust-vectoring control actuation system hardware the thrust-vectoring paddle rates ($\dot{\delta}_{L1}$, $\dot{\delta}_{L2}$, and $\dot{\delta}_{L3}$) are bounded within an interval of ± 120 deg/s.

IV. NDI Controller Design

For the aircraft considered here, two separate controllers are designed. One of the controllers manipulates the aerodynamic control effectors only and the other controller manipulates the thrust-vectoring paddles only. This is done to investigate the maneuvering performance of the aircraft using the aerodynamic controller only and the possibility of maneuvering performance enhancement with the addition of the thrust vector controller. The thrust vector controller is designed to be turned on whenever the aerodynamic controller loses its effectiveness due to excessive angle of attack values. Therefore, when the thrust vector controller is turned on, the aerodynamic controller is turned off and the aerodynamic control effectors are retracted to their neutral positions. In such a case, the aircraft is controlled only by using the total thrusts T_L and T_R created by the two engines and the thrust vector deviation angle pairs $\{\psi_L, \theta_L\}$ and $\{\psi_R, \theta_R\}$.

In the case of TVC, using the dynamic inversion control law in association with Eqs. (4) and (15), the command values for the forces to be created by the left and right engines can be calculated using the following equation for a commanded acceleration state of the aircraft:

$$\hat{G} \begin{bmatrix} \bar{F}^{(b)}_{L\text{com}} \\ \bar{F}^{(b)}_{R\text{com}} \end{bmatrix} = \hat{H}^{-1} \left\{ \begin{bmatrix} \begin{bmatrix} \dot{u}_{\text{com}} & \dot{v}_{\text{com}} & \dot{w}_{\text{com}} \end{bmatrix}^T \\ \begin{bmatrix} \dot{p}_{\text{com}} & \dot{q}_{\text{com}} & \dot{r}_{\text{com}} \end{bmatrix}^T \end{bmatrix} - \bar{F} \right\} - \begin{bmatrix} \bar{F}^{(b)}_a \\ \bar{M}^{(b)}_a \end{bmatrix} \tag{36}$$

However, $\hat{G}$ happens to be an ever singular matrix. This is because it involves the skew symmetric cross-product matrices corresponding to the vectors $\bar{r}^{(b)}_{be_L}$ and $\bar{r}^{(b)}_{be_R}$, which are singular with rank 2. Therefore, $\hat{G}$ is also a rank-deficient matrix. This rank deficiency can be handled as described below. To start with, Eq. (36) can be written again as follows:

$$\hat{G} \begin{bmatrix} \bar{F}^{(b)}_{L\text{com}} \\ \bar{F}^{(b)}_{R\text{com}} \end{bmatrix} = \begin{bmatrix} \bar{F}^{(b)}_{\text{com}} \\ \bar{M}^{(b)}_{\text{com}} \end{bmatrix} \tag{37}$$

where $\bar{F}^{(b)}_{\text{com}}$ and $\bar{M}^{(b)}_{\text{com}}$ are the necessary force and moment vectors in order to realize the commanded accelerations completely.

The consistency of Eq. (37) can be satisfied by allowing freedom for certain components of $\bar{F}^{(b)}_{\text{com}}$ and $\bar{M}^{(b)}_{\text{com}}$. Because the left and right engine nozzle exit locations are symmetric with respect to the centerline of the aircraft, their position vectors can be expressed as $\bar{r}^{(b)}_{be_L} = [e_x e_y e_z]^T$ and $\bar{r}^{(b)}_{be_R} = [e_x - e_y e_z]^T$. Plugging these expressions into Eq. (37), the following constraint equation can be found:

$$M^{(b)}_{y\text{com}} = -e_x F^{(b)}_{z\text{com}} + e_z F^{(b)}_{x\text{com}} \tag{38}$$

This, in turn, necessitates allowing freedom for certain components of the commanded translational and angular acceleration vectors. More specifically, only *two* of the *three* acceleration components $(\dot{u}, \dot{w}, \dot{q})$ can be commanded arbitrarily; the third one must obey the consistency constraint dictated by Eq. (38). That is,

$$J_y\dot{q}_{\text{com}} + e_x m\dot{w}_{\text{com}} - e_z m\dot{u}_{\text{com}} = -\Delta M_y - e_x\Delta F_z + e_z\Delta F_x \quad (39)$$

Furthermore, in return for this restriction, the y components of $\boldsymbol{F}_{L\text{com}}$ and $\boldsymbol{F}_{R\text{com}}$ can be chosen arbitrarily such that their sum will be equal to the y component of $\bar{F}^{(b)}_{\text{com}}$. Here, they are chosen to be equal to each other. In Eq. (39), J_y is the inertia component of the aircraft along the y direction of the body fixed frame, m is the mass of the aircraft, and ΔM_y, ΔF_z, and ΔF_x originate from Eq. (36). They are expressed as

$$\Delta F_x = mV[q\sin(\alpha)\cos(\beta) - r\sin(\beta)] + mg\sin(\theta) - F^{(b)}_{ax} \quad (40)$$

$$\Delta F_z = mV[p\sin(\beta) - q\cos(\alpha)\cos(\beta)] - mg\cos(\theta)\cos(\phi) - F^{(b)}_{az} \quad (41)$$

$$\Delta M_y = (J_x - J_z)pr + J_{xz}(p^2 - r^2) - M^{(b)}_{ay} \quad (42)$$

The angle of attack control of the aircraft necessitates specifying the acceleration command $\dot{w}_{\text{com}}$. Similarly, the pitching maneuver control of the aircraft for a desired pitch angle necessitates specifying the acceleration command $\dot{q}_{\text{com}}$. On the other hand, for the speed control of the aircraft in both of the previous control requirements, it is always necessary to specify the acceleration command $\dot{u}_{\text{com}}$. Therefore, to apply the angle of attack control, the acceleration commands $\dot{u}_{\text{com}}$ and $\dot{w}_{\text{com}}$ are generated and the corresponding $\dot{q}_{\text{com}}$ is found depending on them according to Eq. (39). Alternatively, if a pitching maneuver is required, the acceleration commands $\dot{u}_{\text{com}}$ and $\dot{q}_{\text{com}}$ are generated and the corresponding $\dot{w}_{\text{com}}$ is found depending on them again according to Eq. (39). Hence, $\bar{F}^{(b)}_{\text{com}}$ and $\bar{M}^{(b)}_{\text{com}}$ are determined using Eq. (36) with Eq. (37), which then lead to $\bar{F}^{(b)}_{L}$ and $\bar{F}^{(b)}_{R}$ as shown in Table 1. Afterward, their spherical components $\{T_L, \psi_L, \theta_L\}$ and $\{T_R, \psi_R, \theta_R\}$ can also be determined.

The desired high-α rapid maneuvers, such as Cobra and Herbst maneuvers, are achieved by controlling the yaw–pitch–roll attitude of the aircraft. Thus, the relation of $\bar{F}^{(b)}_{\text{com}}$ and $\bar{M}^{(b)}_{\text{com}}$ to $\bar{F}^{(b)}_{L\text{com}}$ and $\bar{F}^{(b)}_{R\text{com}}$ will obey the constraint equation for the pitching maneuver shown in Table 1.

$\bar{F}^{(b)}_{\text{com}}$ and $\bar{M}^{(b)}_{\text{com}}$ are calculated using Eq. (37) and the commanded accelerations shown in Eq. (36). These accelerations should be directly related to the desired attitude angles, that is, the roll, pitch, and yaw angles of the aircraft. This relation is produced by designing a controller generating the commanded accelerations using the desired and actual attitude angles.

To calculate the commanded angular accelerations, the commanded angular velocities should be calculated first. Thus, the controller is divided into two segments. The first one for the slowly changing dynamics generates the commanded roll, pitch, and yaw angular velocities and the second one for the fast changing dynamics generates the commanded angular accelerations using the commanded and actual angular velocities. Different controller structures can be used for this purpose. A commonly used one is the PI control structure. It is particularly popular for its ease of implementation and for its proven performance in the NDI literature using fighter aircraft examples [16,25,26]. Throughout the present study, PI control structure is used for the slowly changing dynamics. As for the fast changing dynamics, P control structure is used to create an effective derivative action on the PI controller.

For the controller, the error vector $\bar{e}_r(t)$ is defined as the difference between the desired (d) and the actual values of the attitude angles of the aircraft, that is,

$$\bar{e}_r(t) = \begin{bmatrix} \phi_d(t) \\ \theta_d(t) \\ \psi_d(t) \end{bmatrix} - \begin{bmatrix} \phi(t) \\ \theta(t) \\ \psi(t) \end{bmatrix} \quad (43)$$

Implementing the PI controller with the constant gain matrices $\hat{K}_p = \text{diag}(K_{p\phi}, K_{p\theta}, K_{p\psi})$ and $\hat{K}_i = \text{diag}(K_{i\phi}, K_{i\theta}, K_{i\psi})$, the commanded roll, pitch, and yaw angular velocities can be expressed as

$$\begin{bmatrix} \dot{\phi}_{\text{com}}(t) \\ \dot{\theta}_{\text{com}}(t) \\ \dot{\psi}_{\text{com}}(t) \end{bmatrix} = \hat{K}_p\bar{e}_r(t) + \hat{K}_i\int_0^t \bar{e}_r(t')\,\mathrm{d}t' \quad (44)$$

Using Eqs. (8) and (44), the commanded angular velocity components p_{com}, q_{com}, and r_{com} can be calculated. Then, the second error vector $\bar{e}_{\text{av}}(t)$ is defined as the difference between the commanded (com) and the actual values of the body angular velocity components, that is,

$$\bar{e}_{\text{av}}(t) = \begin{bmatrix} p_{\text{com}}(t) \\ q_{\text{com}}(t) \\ r_{\text{com}}(t) \end{bmatrix} - \begin{bmatrix} p(t) \\ q(t) \\ r(t) \end{bmatrix} \quad (45)$$

Implementing the P controller with the gain matrix $\hat{K}_d = \text{diag}(K_{d\phi}, K_{d\theta}, K_{d\psi})$ the commanded angular accelerations $\dot{p}_{\text{com}}$, $\dot{q}_{\text{com}}$, and $\dot{r}_{\text{com}}$ can be expressed as

$$\begin{bmatrix} \dot{p}_{\text{com}}(t) \\ \dot{q}_{\text{com}}(t) \\ \dot{r}_{\text{com}}(t) \end{bmatrix} = \hat{K}_d\bar{e}_{\text{av}}(t) \quad (46)$$

After calculating $\dot{p}_{\text{com}}$, $\dot{q}_{\text{com}}$, and $\dot{r}_{\text{com}}$, $\bar{F}^{(b)}_{\text{com}}$ and $\bar{M}^{(b)}_{\text{com}}$ are determined using Eqs. (36) and (37), which then lead to $\bar{F}^{(b)}_{L}$ and $\bar{F}^{(b)}_{R}$ according to Table 1. $\bar{F}^{(b)}_{L}$ and $\bar{F}^{(b)}_{R}$ are then used to calculate the left and right thrust magnitudes $T_{L\text{com}}$ and $T_{R\text{com}}$ and the thrust-vectoring angle pairs $\{\psi_{L\text{com}}, \theta_{L\text{com}}\}$ and $\{\psi_{R\text{com}}, \theta_{R\text{com}}\}$. Finally, the throttle deflections and the six thrust-vectoring paddle angles can be calculated from them.

The block diagram representation of the proposed thrust vector controller that works to achieve the desired attitude of the aircraft is shown jointly in Figs. 7 and 8.

Assuming that there are no uncertainties and no saturations due to control effector limitations, the NDI approach produces a linear system of three independent *free integrators* involving the angular accelerations $\dot{p}_{\text{com}}$, $\dot{q}_{\text{com}}$, and $\dot{r}_{\text{com}}$. Using these assumptions and combining the block diagrams shown in Figs. 7 and 8, the closed-loop transfer functions can be written as follows:

$$\frac{\phi(s)}{\phi_d(s)} = \frac{K_{d\phi}(K_{p\phi}s + K_{i\phi})}{s^3 + K_{d\phi}s^2 + K_{p\phi}K_{d\phi}s + K_{i\phi}K_{d\phi}} \quad (47a)$$

Table 1 Achievable desired forces and moments by TVC engines

Constraint equation for pitching maneuver	Constraint equation for angle of attack control
$F^{(b)}_{\text{com}z} = \left(-M^{(b)}_{\text{com}y} + e_z F^{(b)}_{\text{com}x}\right)/e_x$	$M^{(b)}_{\text{com}y} = -e_x F^{(b)}_{\text{com}z} + e_z F^{(b)}_{\text{com}x}$
$F^{(b)}_{L\text{com}x} = \left(F^{(b)}_{\text{com}x} - (M^{(b)}_{\text{com}z} - e_x F^{(b)}_{\text{com}y})/e_y\right)\Big/2$, $F^{(b)}_{R\text{com}x} = \left(F^{(b)}_{\text{com}x} + (M^{(b)}_{\text{com}z} - e_x F^{(b)}_{\text{com}y})/e_y\right)\Big/2$	
$F^{(b)}_{L\text{com}y} = F^{(b)}_{R\text{com}y} = F^{(b)}_{\text{com}y}/2$	
$F^{(b)}_{L\text{com}z} = \left(F^{(b)}_{\text{com}z} + (M^{(b)}_{\text{com}x} + e_z F^{(b)}_{\text{com}y})/e_y\right)/2$, $F^{(b)}_{R\text{com}z} = \left(F^{(b)}_{\text{com}z} - (M^{(b)}_{\text{com}x} + e_z F^{(b)}_{\text{com}y})\Big/e_y\right)/2$	

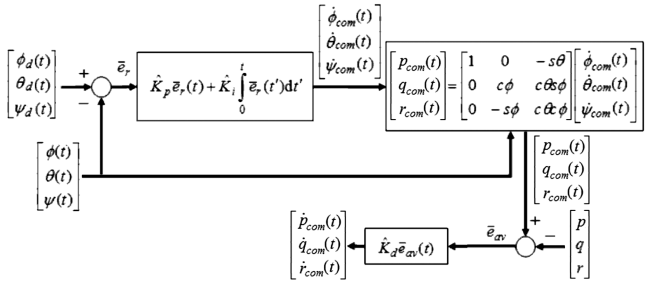

Fig. 7 The block diagram for commanded angular accelerations.

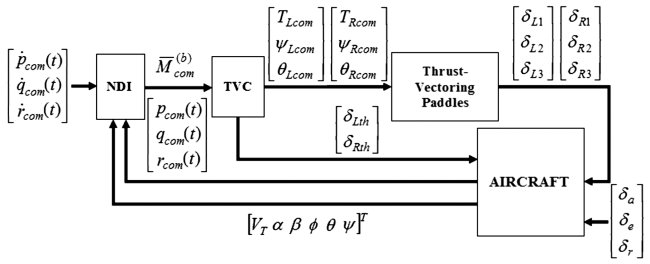

Fig. 8 The block diagram of NDI for the angular velocities.

$$\frac{\theta(s)}{\theta_d(s)} = \frac{K_{d\theta}(K_{p\theta}s + K_{i\theta})}{s^3 + K_{d\theta}s^2 + K_{p\theta}K_{d\theta}s + K_{i\theta}K_{d\theta}} \tag{47b}$$

$$\frac{\psi(s)}{\psi_d(s)} = \frac{K_{d\psi}(K_{p\psi}s + K_{i\psi})}{s^3 + K_{d\psi}s^2 + K_{p\psi}K_{d\psi}s + K_{i\psi}K_{d\psi}} \tag{47c}$$

To calculate $\hat{K}_p$, $\hat{K}_i$, and $\hat{K}_d$, the poles of the desired closed-loop dynamics of the attitude angles should be specified. Here, these poles are specified as

$$\left\{-\omega_{n\phi}(\zeta_\phi \pm j\sqrt{1-\zeta_\phi^2}), -\omega'_{n\phi}\right\}$$
$$\left\{-\omega_{n\theta}(\zeta_\theta \pm j\sqrt{1-\zeta_\theta^2}), -\omega'_{n\theta}\right\}$$
$$\left\{-\omega_{n\psi}(\zeta_\psi \pm j\sqrt{1-\zeta_\psi^2}), -\omega'_{n\psi}\right\}$$

These poles are selected here according to the desired flying and handling qualities of the aircraft. They are selected considering the military documentations Mil-F-8785-C [27] and Mil-STD 1797-A [28]. As for the poles of the roll motion, they are selected considering some additional studies [29–31] as well. The first of these studies [29] introduces criteria on time response specifications for rapid maneuvering as described in Fig. 9. The other two [30,31] introduce criteria on responsiveness for precision tracking as described in Fig. 10.

Using the selected poles and Eqs. (47a–47c), the controller gain matrices are found as follows:

$$\hat{K}_d = \mathrm{diag}(2\zeta_\phi\omega_{n\phi} + \omega'_{n\phi}, 2\zeta_\theta\omega_{n\theta} + \omega'_{n\theta}, 2\zeta_\psi\omega_{n\psi} + \omega'_{n\psi}) \tag{48a}$$

$$\hat{K}_p = \mathrm{diag}\left(\frac{\omega_{n\phi}(\omega_{n\phi} + 2\zeta_\phi\omega'_{n\phi})}{2\zeta_\phi\omega_{n\phi} + \omega'_{n\phi}}, \frac{\omega_{n\theta}(\omega_{n\theta} + 2\zeta_\theta\omega'_{n\theta})}{2\zeta_\theta\omega_{n\theta} + \omega'_{n\theta}}, \frac{\omega_{n\psi}(\omega_{n\psi} + 2\zeta_\psi\omega'_{n\psi})}{2\zeta_\psi\omega_{n\psi} + \omega'_{n\psi}}\right) \tag{48b}$$

$$\hat{K}_i = \mathrm{diag}\left(\frac{\omega^2_{n\phi}\omega'_{n\phi}}{2\zeta_\phi\omega_{n\phi} + \omega'_{n\phi}}, \frac{\omega^2_{n\theta}\omega'_{n\theta}}{2\zeta_\theta\omega_{n\theta} + \omega'_{n\theta}}, \frac{\omega^2_{n\psi}\omega'_{n\psi}}{2\zeta_\psi\omega_{n\psi} + \omega'_{n\psi}}\right) \tag{48c}$$

V. Comparison of Aerodynamic Control and Thrust Vector Control at High-α Maneuvers

The controller design for high-α maneuvers is essentially based on attitude and angular velocity control of the aircraft. For longitudinal maneuvers of the aircraft only pitching motion is controlled. The lateral maneuvers are controlled by generating the coordinated yawing and rolling motion commands. Before starting the maneuvers, it is assumed that the aircraft has been at wings level steady flight at 5000 m altitude and 0.75 M with $\alpha_0 = 0.70$ deg, $\delta_{e0} = -1.29$ deg, $T_{L0} = T_{R0} = 22,860$ N, and $\delta_{L\mathrm{th}} = \delta_{R\mathrm{th}} = 0.54$.

A. Pull-Up Maneuver for Stall Testing

Simulation of such a maneuver is desirable to identify the stall regions described in Sec. III.B. This maneuver is realized using the elevator so that the aircraft starts to climb up from the initial altitude. The time histories of the elevator command, the total velocity, the angle of attack, and the pitch angle for this maneuver are shown in Figs. 11 and 12. For the initial conditions considered here, the simulation shows that the aircraft is in stall after the seventh second; up to the 13th second it is in the post-stall region, and afterward the deep stall region starts. When the aircraft is in the deep stall region, although there is still an elevator command trying to pull the aircraft up, there occurs the undesired nose-down pitching motion which

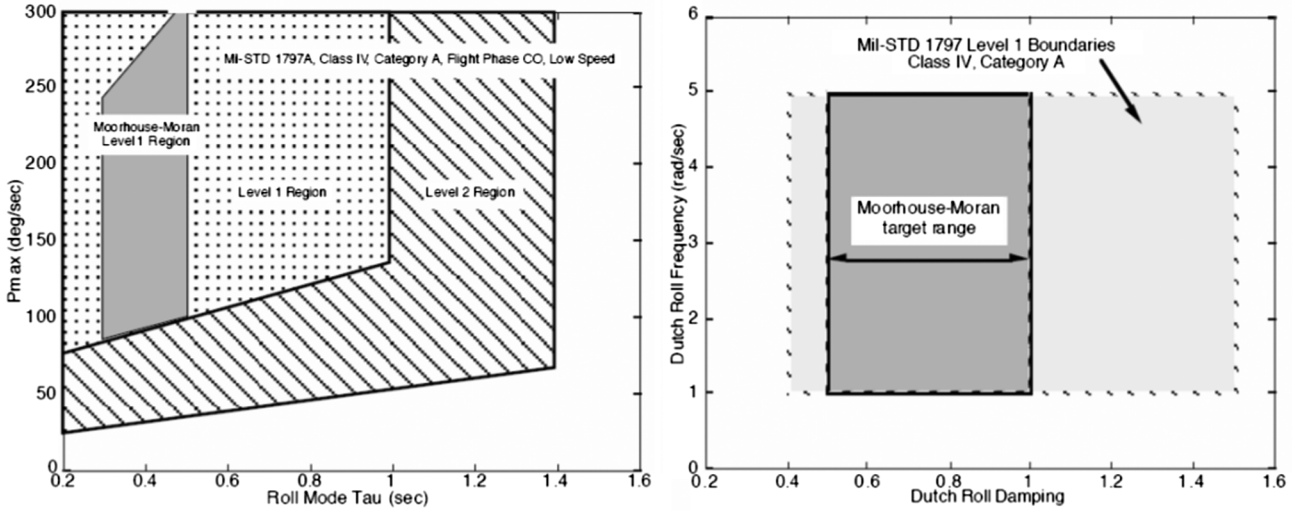

Fig. 9 Roll and dutch roll mode specifications for low angle of attach (left) and fighter aircrafts (right).

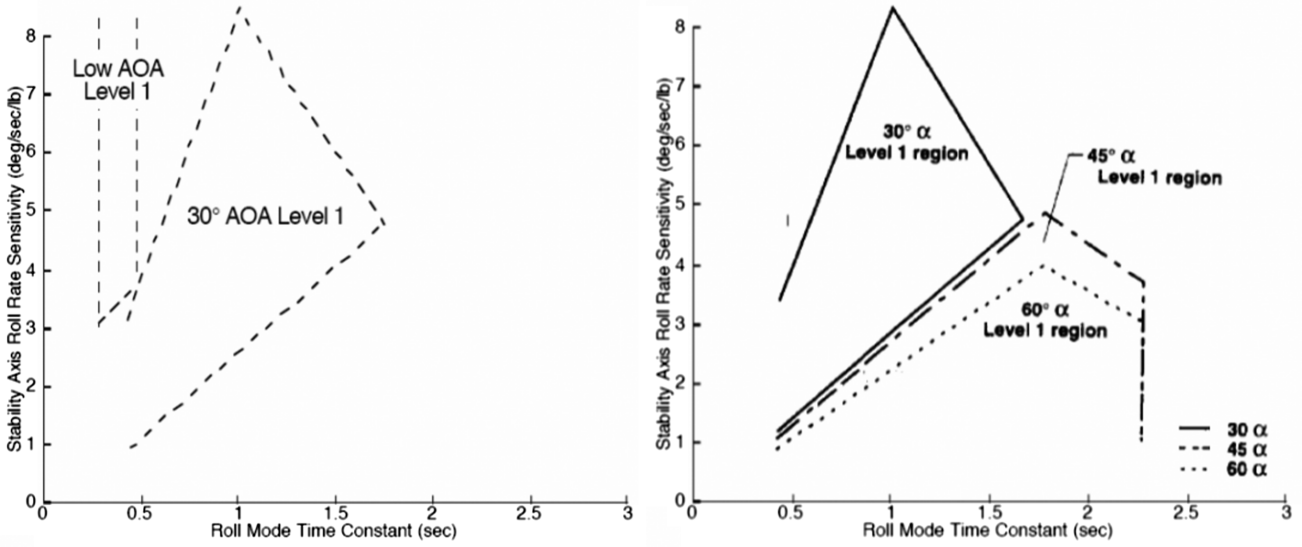

Fig. 10 Roll mode specifications for precision tracking.

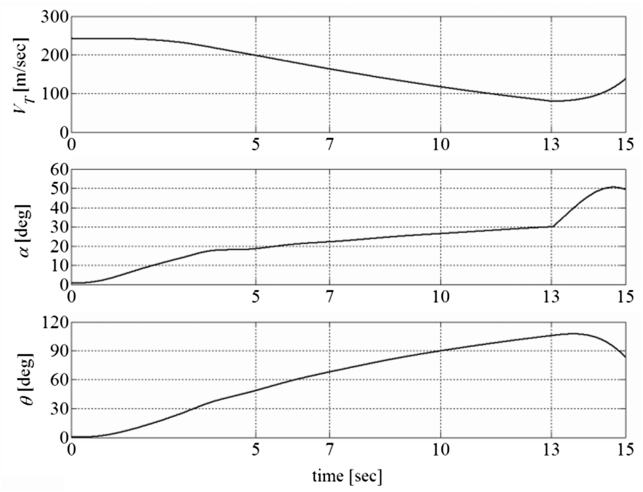

Fig. 11 The states for stall manipulation in longitudinal plane of motion.

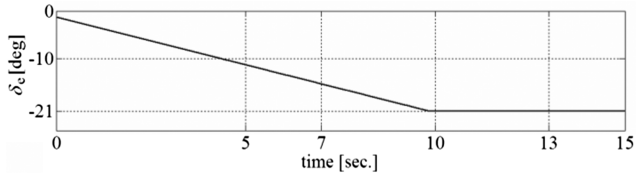

Fig. 12 The elevator deflection for stall manipulation.

develops very rapidly. This simulation suggests that the thrust vectoring should start at the latest just before entering the deep stall region.

B. Cobra Maneuver

The Cobra maneuver was first demonstrated by the Russian pilot Pougachev. This maneuver is composed of two successive phases. In the first *pull-up* phase the pilot makes a nose-up maneuver until the aircraft gets into stall and therefore slows down dramatically. In the second *recovery* phase the pilot starts the nose-down maneuver and returns the aircraft to a desired pitch angle. The pull-up phase of the maneuver is realized by the aerodynamic control surfaces and the recovery phase of the maneuver can be realized by means of either aerodynamic control only or TVC only. The performances of these two controls are compared in the sequel.

1. *Aerodynamic Control Only*

In this case, for commanded accelerations and undeflected TVC paddles, Eq. (15) is solved for the aerodynamic forces and moments as

$$\begin{bmatrix} \bar{F}^{(b)}_{a\text{com}} \\ \bar{M}^{(b)}_{a\text{com}} \end{bmatrix} = \hat{H}^{-1} \left\{ \begin{bmatrix} [\,\dot{u}_{\text{com}} & \dot{v}_{\text{com}} & \dot{w}_{\text{com}}\,]^T \\ [\,\dot{p}_{\text{com}} & \dot{q}_{\text{com}} & \dot{r}_{\text{com}}\,]^T \end{bmatrix} - \bar{F} \right\} - \hat{G} \begin{bmatrix} [\,T_L & 0 & 0\,]^T \\ [\,T_R & 0 & 0\,]^T \end{bmatrix} \tag{49}$$

For the purpose of yaw–pitch–roll attitude maneuver, the aerodynamic control surface deflections $(\delta_{a\text{com}}, \delta_{e\text{com}}, \delta_{r\text{com}})$ are found from $\bar{M}^{(b)}_{a\text{com}}$. On the other hand, the aerodynamic moments are expressed as $M^{(b)}_{ax} = (Q_d Sb)C_l$, $M^{(b)}_{ay} = (Q_d S\bar{c})C_m$, $M^{(b)}_{az} = (Q_d Sb)C_n$, where

$$C_l = C'_l(\alpha, \beta, p, q, r) + C_{l\delta_a}(\alpha, \beta)\delta_a + C_{l\delta_r}(\alpha, \beta)\delta_r$$
$$C_m = C'_m(\alpha, \beta, p, q, r) + C_{m\delta_e}(\alpha, \beta)\delta_e$$
$$C_n = C'_n(\alpha, \beta, p, q, r) + C_{n\delta_a}(\alpha, \beta)\delta_a + C_{n\delta_r}(\alpha, \beta)\delta_r$$

Q_d is the dynamic pressure, S is the surface area of the wing planform, $\bar{c}$ is the mean chord length, and b is the span of the wing. Thus, the commanded aerodynamic control surface deflections can be calculated as

$$\begin{bmatrix} \delta_{a\text{com}} \\ \delta_{e\text{com}} \\ \delta_{r\text{com}} \end{bmatrix} = \begin{bmatrix} C_{l\delta_a} & 0 & C_{l\delta_r} \\ 0 & C_{m\delta_e} & 0 \\ C_{n\delta_a} & 0 & C_{n\delta_r} \end{bmatrix}^{-1} \begin{bmatrix} M^{(b)}_{ax\text{com}}/(Q_d Sb) - C'_l \\ M^{(b)}_{ay\text{com}}/(Q_d S\bar{c}) - C'_m \\ M^{(b)}_{az\text{com}}/(Q_d Sb) - C'_n \end{bmatrix} \tag{50}$$

As for the mechanization, the actuation dynamics for the aerodynamic control surfaces is modeled as follows:

$$\begin{bmatrix} \dot{\delta}_a \\ \dot{\delta}_e \\ \dot{\delta}_r \end{bmatrix} = (2\pi f_{nA}) \left\{ \begin{bmatrix} \delta_{a\text{com}} \\ \delta_{e\text{com}} \\ \delta_{r\text{com}} \end{bmatrix} - \begin{bmatrix} \delta_a \\ \delta_e \\ \delta_r \end{bmatrix} \right\} \tag{51}$$

Here $f_{nA} = 30$ Hz and the commanded values are determined by Eq. (50). To ensure the physical limits of the aerodynamic control actuation system hardware the aerodynamic control surface rates ($\dot{\delta}_a$, $\dot{\delta}_e$, and $\dot{\delta}_r$) are bounded within an interval of ± 45 deg/s.

In the simulations, the pull-up phase of the Cobra maneuver is started at the specified initial condition and the aircraft climbs up from the initial altitude. After the eighth second when the aircraft is in

stall, with $\alpha = 23$ deg and $\theta = 76$ deg, the recovery phase of the maneuver is started using the aerodynamic controls only. In the recovery phase the pitch angle of the aircraft is brought to a desired value of -5 deg in 18 s. The simulations showed that, if the recovery phase is started beyond $\alpha = 23$ deg, the desired maneuver cannot be achieved without any saturation of the elevator deflection. Hence, considering the specified initial conditions, the recovery phase should start at latest when $\alpha = 23$ deg so that the desired maneuver can be achieved using the aerodynamic controls only. The time histories of the total velocity, the angle of attack, the pitch angle, and the elevator deflection are shown in Figs. 13 and 14 in a case where the aerodynamic control is used successfully in the recovery phase.

2. TVC Control Only

In the simulations, the pull-up phase of the maneuver is started at the same initial condition and the aircraft climbs up from the initial altitude. After the 13th second when the aircraft gets into the deep stall region, with $\alpha = 30$ deg and $\theta = 105$ deg, the recovery phase of the maneuver is started using TVC only. In the recovery phase, the pitch angle of the aircraft is brought to a desired value of -5 deg in 18 s. The simulations showed that, using TVC instead of aerodynamic control, the maneuvering capability of the aircraft is enhanced and the recovery phase of the maneuver could be started at higher angles of attack when the pitch angles are also higher than the case with "aerodynamic control only." The time histories of the total velocity, the angle of attack, the pitch angle, and the thrust-vectoring paddle deflections are shown in Figs. 15 and 16.

C. Herbst Maneuver

The Herbst maneuver is named after W. B. Herbst, proponent of using post-stall flight in air combat. It is used for heading reversal of the aircraft with a downward nose pointing for a possible dive attack in close air combat.

The Herbst maneuver is composed of two successive phases. In the first pull-up phase, the aircraft makes a nose-up maneuver until it gets into stall and therefore slows down dramatically. In the second *heading reversal* phase, the aircraft starts a roll motion coordinated with a yaw motion to change its heading and to lower its pitch angle. At the end of the maneuver, the aircraft turns 180 deg and thus reverses its initial heading direction at the beginning of the maneuver and meanwhile assumes a desired pitch angle. The pull-up phase of the maneuver is realized by the aerodynamic control surfaces. However, the heading reversal phase of the maneuver can only be realized by means of TVC. This conclusion has been reached based on the results of the simulations explained in the sequel.

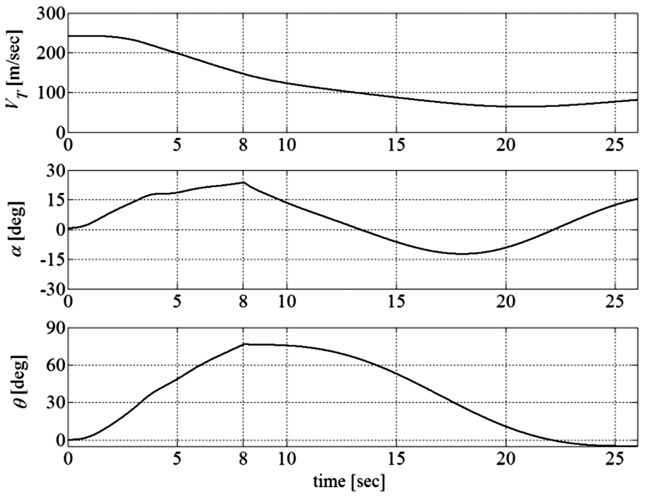

Fig. 13 The states for the Cobra maneuver in longitudinal plane of motion, aerodynamic control.

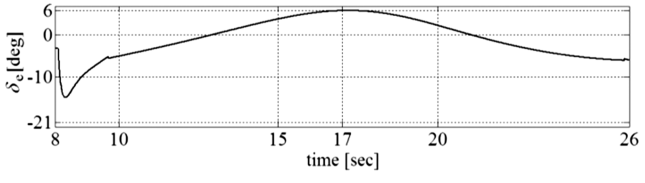

Fig. 14 The elevator deflection for the Cobra maneuver.

1. TVC Control Only

In the simulations, the pull-up phase of the Herbst maneuver is started at the same initial condition and the aircraft climbs up from the initial altitude. After the 12th second when the aircraft is in the post-stall region, with $\alpha = 28$ deg and $\theta = 101$ deg, the heading reversal phase of the maneuver is started using TVC only. In the heading reversal phase, a coordinated lateral maneuver is realized by commanding the roll angle to -30 deg and the yaw rate to -18 deg/s in 15 s. At the same time, the pitch angle of the aircraft is brought to a desired value of -12 deg in 18 s.

The time histories of the total velocity, the angle of attack, the side slip angle, the roll, pitch, and yaw angles, and the thrust-vectoring paddle deflections for this maneuver are shown in Figs. 17–19.

2. Aerodynamic Control Only

In the simulations, the pull-up phase of the Herbst maneuver is started at the specified initial condition and the aircraft climbs up from the initial altitude. The simulations showed that, if the heading

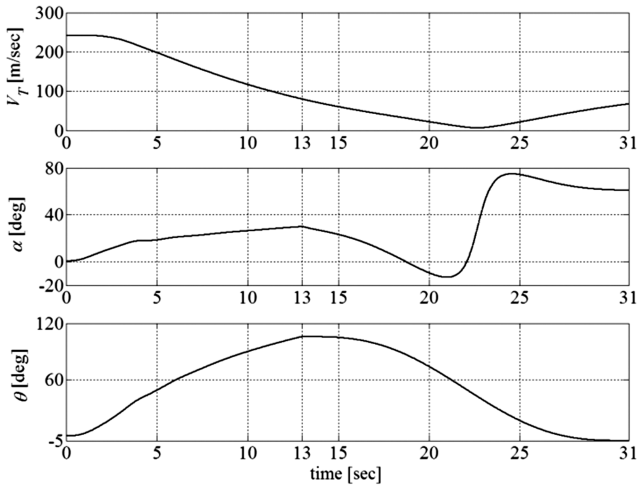

Fig. 15 The states for the Cobra maneuver in the longitudinal plane of motion, TVC.

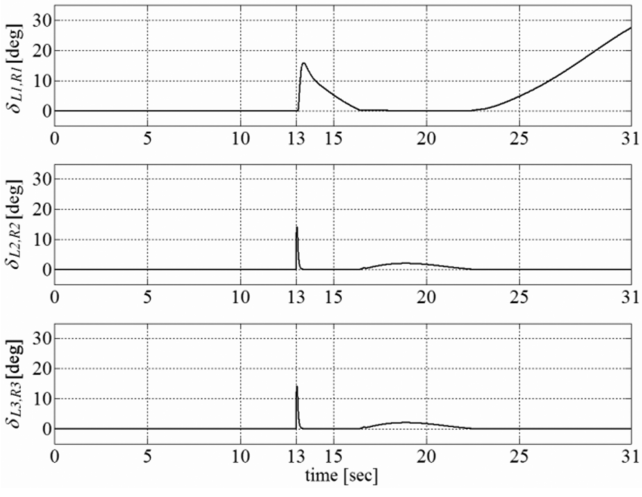

Fig. 16 TVC paddle deflections for the Cobra maneuver.

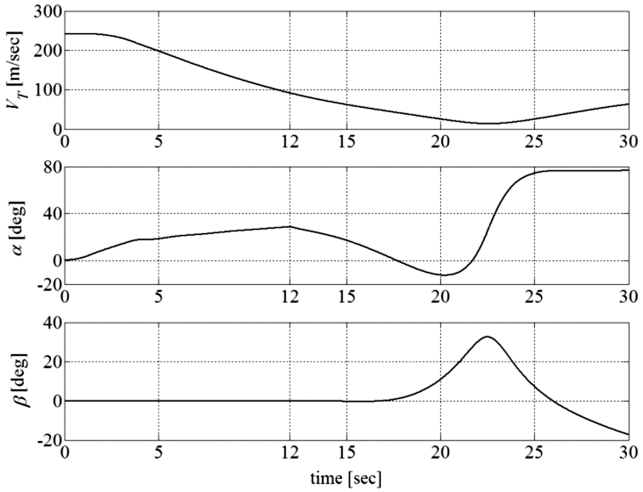

Fig. 17 The translational states for the Herbst maneuver, TVC control.

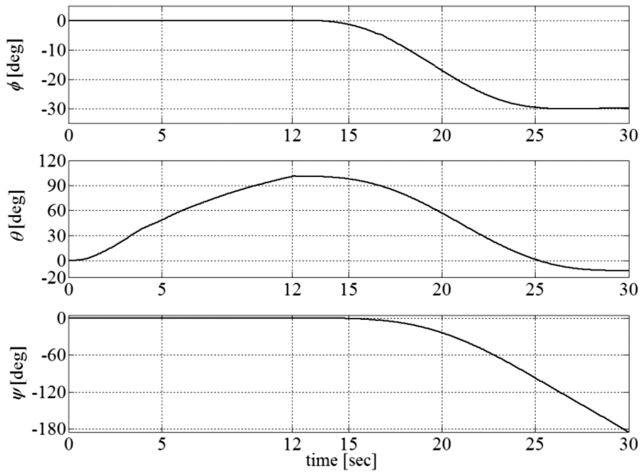

Fig. 18 The rotational states for the Herbst maneuver, TVC control.

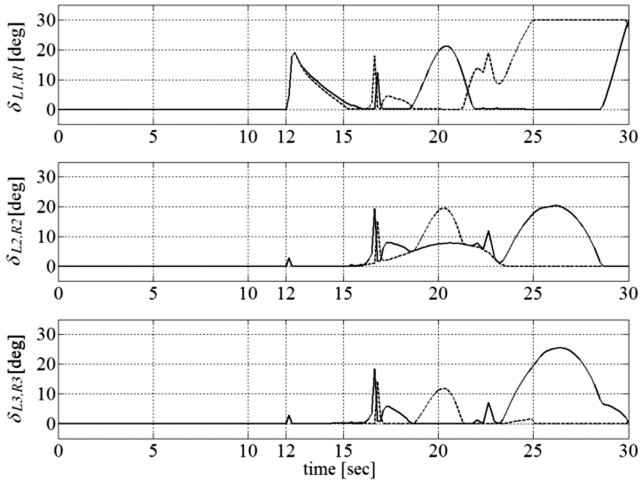

Fig. 19 TVC paddle deflections for the Herbst maneuver. (The dotted lines are for the left engine paddles).

reversal phase is started beyond $\alpha = 14$ deg, the desired maneuver cannot be achieved without any saturation of the aerodynamic control surfaces. Hence, considering the specified initial conditions, the second phase of the maneuver can be started when $\alpha \leq 14$ deg. It is also noticed that, although the desired roll and pitch angles are achieved at the end of the maneuver, a complete heading reversal cannot be realized as desired. This is because the yaw rate can only be commanded up to a limited value without any saturation of the aerodynamic control surfaces. This is demonstrated with a specific simulation, where the second phase is started when $\alpha = 14$ deg and $\theta = 26$ deg. In this simulation, the roll angle is commanded to a desired value of -30 deg at 15 s and the pitch attitude is commanded to a desired value of -12 deg at 18 s. However, it is seen that the yaw rate can only be commanded at most to a value of -4.5 deg/s due to saturations, which happens to be insufficient for a complete heading reversal. The time histories of the total velocity, the angle of attack, the side slip angle, the roll, pitch, and yaw angles, and the commanded aileron, elevator, and rudder deflections are shown in Figs. 20–22.

As verified by simulations, the achieved maneuvering capability using the "aerodynamic control only" is very low when compared to the case with "TVC only." A desired maneuver with complete heading reversal cannot be realized by using the aerodynamic control surfaces only. The aerodynamic control surfaces turn out to be extremely inadequate for this purpose.

VI. Conclusions

This study focuses on high-α flight maneuverability and air combat superiority enhancement of a conventionally controlled fighter–bomber aircraft using *thrust-vectoring control* system integration. Two basic air superiority maneuvers are studied as test cases; the *Cobra maneuver* with longitudinal motion only and the

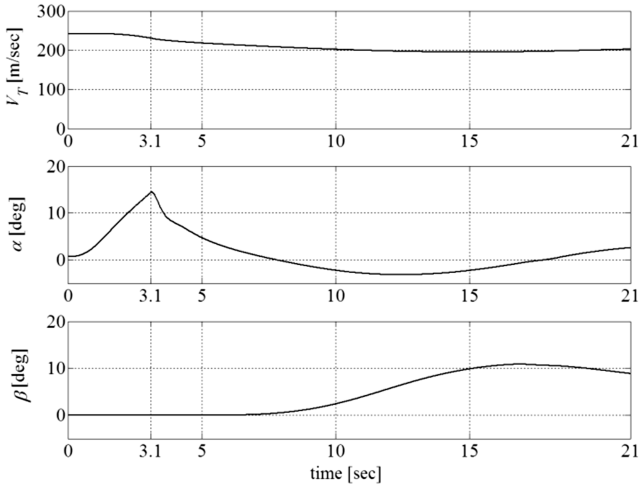

Fig. 20 The translational states for the Herbst maneuver attempt, aerodynamic control.

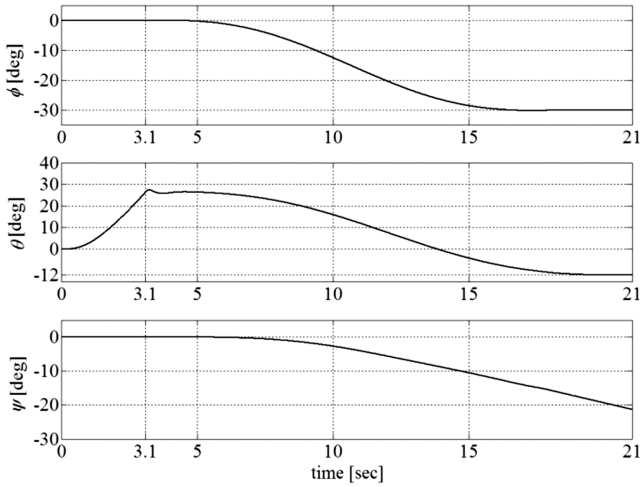

Fig. 21 The rotational states for the Herbst maneuver attempt, aerodynamic control.

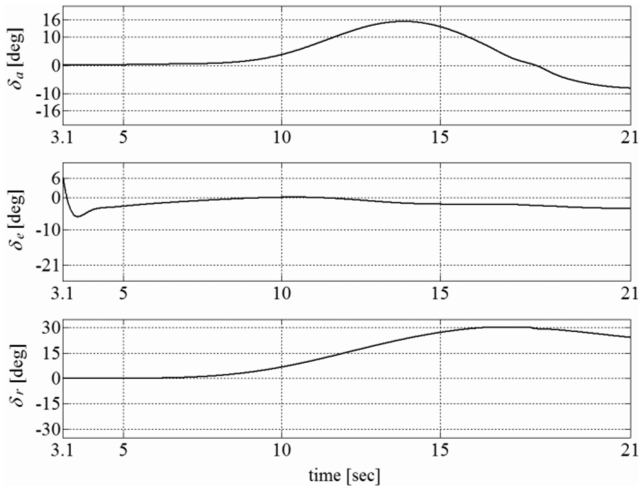

Fig. 22 The aerodynamic control surfaces deflections for the Herbst maneuver attempt.

Herbst maneuver with both longitudinal and lateral motions. The 6 DoF (degree of freedom) nonlinear flight dynamics model, nonlinear aerodynamics model, engine model, and the model of the thrust-vectoring paddles with control actuation system mechanization are built for simulation. High angle of attack aerodynamics of the aircraft is studied and the integrated Bihrle–Weissmann chart is plotted to analyze the departure and stall susceptible regions.

The controller design is carried out by applying the NDI methodology using PI with a rate feedback control structure. After a few trials, the following set of control parameters have been found to be satisfactory: $\omega_{n\theta} = \omega_{n\psi} = \omega_{n\phi} = 2\pi$ rad/s, $\omega'_{n\theta} = \omega'_{n\psi} = \omega'_{n\phi} = 14\pi$ rad/s, and $\zeta_\theta = \zeta_\psi = \zeta_\phi = 1$.

The desired Cobra maneuver is simulated using either the aerodynamic control only or the TVC only. It is seen that, only under limited conditions the maneuver can be achieved by using the aerodynamic control only. Hence, it is concluded that the elevator control is ineffective to realize the desired maneuver at higher values of angle of attack and therefore TVC should be used instead.

As for the Herbst maneuver, the simulations have shown that the aerodynamic control by itself is totally unqualified. The maneuver cannot be started beyond $\alpha = 14$ deg and at that value the aircraft is not even in stall yet. Even then, adequate yaw rates cannot be commanded due to saturations and the desired complete heading reversal cannot be achieved.

Both of the maneuvers are then simulated using the integrated TVC system. Integration of the thrust-vectoring paddles within the system created notably superior performance on the high angle of attack controllability and rapid maneuverability of the aircraft. It is observed that the recovery phase of the Cobra maneuver can be started even when the aircraft gets into deep stall and the pitch attitude can be commanded from beyond vertical to negative values rapidly in 18 s. As also observed, the heading reversal phase of the Herbst maneuver can be started even when $\alpha = 28$ deg. Consecutively, a complete heading reversal maneuver coordinated with a similar pitch motion as in a Cobra maneuver can be successfully and rapidly realized in 18 s.

Further studies are still being carried out on the subject. Some of these studies are about constructing a departure and stall indication trigger to start the controller action when the aircraft enters the stall susceptible regions, adding atmospheric disturbances such as wind, turbulence and gust models, and considering aerodynamic coefficient uncertainties and sensor noise.

To emphasize the benefits of the TVC integration, various other test cases of high angle of attack rapid maneuvering can also be studied. The following examples can be considered as some of the typical ones of such test cases: the velocity vector roll maneuvers, the maneuvers for pointing the aircraft's nose toward the opponent aircraft, the tail chase acquisition maneuvers, and the maneuvers for the radar zone avoidance.

On the other hand, the human pilot can be modeled and integrated in the control loop to study the effect of the pilot in the performance of the maneuvers. A robust performance analysis of the NDI controller under the effect of atmospheric disturbances, aerodynamic coefficient uncertainties together with the sensor, engine, and observation noises is also a significant topic for further study.

References

[1] Chambers, J. R., "High-Angle-of-Attack Technology: Progress and Challenges," *High-Angle-of-Attack Technology*, NASA CP-3149, Vol. 1, May 1992, pp. 1–22.

[2] Herbst, W. B., "X-31A at First Flight," *Flying Qualities*, AGARD CP-508, Feb. 1991, pp. 29-1–29-8.

[3] Canter, D. E., "X-31 Post-Stall Envelope Expansion and Tactical Utility Testing," *Fourth High Alpha Conference*, NASA CP-10143, Vol. 2, July 1994.

[4] Kidman, D. S., Vickers, J. E., Olson, B. P., and Gerzanics, M. A., "Evaluation of the F-16 Multi-Axis Thrust Vectoring Aircraft," AFFTC TR-95-12, Sept. 1995.

[5] Smith, W., "X-29 High AOA Flight Test Results: An Overview," *SAE Aerospace Atlantic Conference and Exposition*, SAE International, Washington, D.C., April 1993.

[6] Gilbert, W. P., Nguyen, L. T., and Gera, J., "Control Research in the NASA High-Alpha Technology Program," *Aerodynamics of Combat Aircraft Controls and of Ground Effects*, AGARD CP-465, April 1990, pp. 3-1–3-18.

[7] Ogburn, M. E., and Foster, J. V., "Development of High-Angle-of-Attack Nose-Down Pitch Control Margin Design Guidelines for Combat Aircraft," NASA CP-10127, Dec. 1993, pp. 293–322.

[8] "Cooperative Program on Dynamic Wind Tunnel Experiments for Maneuvering Aircraft," AGARD AR-305, Oct. 1996.

[9] Foster, J. V., "Investigation of the Susceptibility of Fighter Airplanes to the Out-of-Control Falling Leaf Mode," NASA Langley Research Center, *NASA High Angle of Attack Conference*, ITAR, Hampton, VA, Sept. 1996.

[10] Kalviste, J., "Math Modeling of Aero Data for Aircraft Dynamic Motion," AIAA Paper 94-AFM-26-7, Aug. 1994.

[11] Smith, P. R., "Functional Control Law Design Using Exact Non-Linear Dynamic Inversion," *AIAA Atmospheric Flight Mechanics Conference*, AIAA, Washington, D.C., Aug. 1994, pp. 481–486; also AIAA Paper 94-3516-CP.

[12] Smith, P. R., and Patel, Y., "Translational Motion Control Of VSTOL Aircraft Using Nonlinear Dynamic Inversion," AIAA Atmospheric Flight Mechanics Conference, AIAA, Washington, D.C., Aug. 1995, pp. 238–252; also AIAA Paper 95-3452-CP.

[13] Ostroff, A. J., and Bacon, B. J., "Force and Moment Approach for Achievable Dynamics Using Nonlinear Dynamic Inversion," AIAA Paper 99-4001, Aug. 1999.

[14] Isidori, A., *Nonlinear Control Systems*, 2nd ed., Springer–Verlag, New York, 1995, Chaps. 3–5.

[15] Bugajski, J. D., and Enns, F. D., "Nonlinear Control Law with Application to High Angle of Attack Flight," *Journal of Guidance, Control, and Dynamics*, Vol. 15, No. 3, 1992, pp. 761–767.

[16] Enns, D., Bugajski, D., Hendrick, R., and Stein, G., "Dynamic Inversion: An Evolving Methodology for Flight Control Design," *International Journal of Control*, Vol. 59, No. 1, 1992, pp. 71–91.

[17] Patel, Y., and Smith, P. R., "Translational Motion Control of Vertical Takeoff Aircraft Using Nonlinear Dynamic Inversion," *Journal of Guidance, Control, and Dynamics*, Vol. 21, No. 1, 1998, pp. 179–182.

[18] Smith, P. R., and Berry, A., "Flight Test Experience of a Non-Linear Dynamic Inversion Control Law on the VAAC Harrier," AIAA Paper 2000-3914, Aug. 2000.

[19] Littleboy, D. M., and Smith, P. R., "Using Bifurcation Methods to Aid Nonlinear Dynamic Inversion Control Law Design," *Journal of Guidance, Control, and Dynamics*, Vol. 21, No. 4, 1998, pp. 632–638.

[20] Snell, A., "Decoupling Control with Applications to Flight," *Journal of Guidance, Control, and Dynamics*, Vol. 21, No. 4, 1998, pp. 647–655.

[21] Durham, W., "Dynamic Inversion and Model-Following Control," AIAA Paper 96-3690, July 1996.

[22] Garza, F. R., and Morelli, E. A., "A Collection of Nonlinear Aircraft Simulations in MATLAB," NASA TM-2003-212145, Jan. 2003.

[23] Nguyen, L. T., Ogburn, M. E., Gilbert, W. P., Kibler, K. S., Brown, P. W., and Deal, P. L., "Simulator Study of Stall/Post-Stall Characteristics of a Fighter Airplane with Relaxed Longitudinal Static Stability," NASA TP 1538, Langley Research Center, 1979.

[24] Bowers, A. H., Pahle, J. W., Wilson, R. J., Flick, B. C., and Rood, R. L., "An Overview of the NASA F-18 High Alpha Research Vehicle," NASA, TM-4772, Research Engineering, NASA Dryden Flight Research Center, 1996.

[25] "Application of Multivariable Control Theory to Aircraft Control Laws: Final Report: Multivariable Control Design Guidelines," WL-TR-96-3099, Flight Dynamics Directorate, Wright Laboratory, Air Force Materiel Command, Wright–Patterson AFB, OH, May 1996.

[26] Ito, D., Georgie, J., Valasek, J., and Ward, D. T., "Re-Entry Vehicle Flight Controls Design Guidelines: Dynamic Inversion," GN&C Design & Analysis Branch NASA Johnson Space Center NAG9-1085, May 2000.

[27] "Military Specification Flying Qualities of Piloted Airplanes," Mil-F-8785-C, Nov. 1980.

[28] "Military Standard—Flying Qualities of Piloted Aircraft," Mil-STD-1797-A, Jan. 1990.

[29] Moorhouse, D. J., and Moran, W. A., "Flying Qualities Design Criteria for Highly Augmented Systems," *IEEE National Aerospace and Electronics Conference*, IEEE, Piscataway, NJ, May 1985.

[30] Kreckler, G. C., Wilson, D. J., and Riley, D. R., "High Angle of Attack Flying Qualities Criteria," AIAA Paper 90-0219, Jan. 1990.

[31] Murphy, P. C., Davidson, J. B., Lallman, F. J., Morelli, E. A., Messina, M. D., Connelly, P. J., and Thomson, M. P., "An Evaluation of Design Methodology and High Alpha Design Criteria for the ANSER Lateral-Directional Control Law," NASA CP-1998-207676 / PT1, *NASA High-Angle-of-Attack Technology Conference*, ITAR, Hampton, VA, Sept. 1996.